minerals

MDPI

Article

Authigenic Green Mica in Interflow Horizons within Late Cretaceous Deccan Volcanic Province, India and Its Genetic Implications

Pragya Singh [1], Santanu Banerjee [1,*], Kanchan Pande [1], Satadru Bhattacharya [2], Subham Sarkar [2] and Emilia Le Pera [3]

[1] Department of Earth Sciences, Indian Institute of Technology Bombay, Powai, Mumbai 400076, India; pragyasingh.vns@gmail.com (P.S.); kanchanpande@iitb.ac.in (K.P.)
[2] Space Applications Centre, Indian Space Research Organisation, Ahmedabad 380015, India; satadru@sac.isro.gov.in (S.B.); subhamrajsarkar@gmail.com (S.S.)
[3] Dipartimento di Biologia, Ecologia e Scienze della Terra, Università della Calabria, Rende, 87036 Cosenza, Italy; emilia.lepera@unical.it
* Correspondence: santanu@iitb.ac.in

Abstract: Green authigenic mica, i.e., celadonite, is commonly associated with submarine alteration of basic igneous rock. However, very few studies have reported the formation of celadonite under nonmarine conditions. An integrated study involving field investigation, petrography, mineralogy, and mineral chemistry highlighted the origin of celadonite in two clay-rich horizons (green boles) of the Late Cretaceous Deccan volcanic province. Within the Salher green bole, the celadonite occurred as the dissolution and alteration of plagioclase, volcanic glass, and pore-filling cement. In the case of the Pune green bole, the celadonite was formed by the alteration of plagioclase, pyroxene, and precipitation as film within intergranular pores, along with zeolite. The celadonite in the Salher green bole exhibited slightly lower K_2O and Fe_2O_3 and higher Al_2O_3 than in the Pune. The mineral chemistry of the former showed a composition closer to ferro-aluminoceladonite. Although the mineral chemistry of celadonite overlaps with glauconite, the distinct 10 Å and 15 Å reflections in XRD, euhedral lath and honeycomb morphology under SEM, and characteristic absorption bands in VNIR spectroscopy (0.4–2.5 µm) and FTIR spectroscopy (400–4000 cm^{-1}) identified celadonite and Fe-smectite within green boles. The green boles were formed either by the alteration of a volcaniclastic deposit in local pools of water or by the in situ alteration of the fragmentary flow top. The present study is significant due to the occurrence of celadonite in a nonmarine environment, as it otherwise forms under submarine conditions.

Keywords: celadonite; Fe-smectite; authigenic minerals; green bole; Deccan volcanic province; volcaniclastic; clay-rich interbasaltic layer

Citation: Singh, P.; Banerjee, S.; Pande, K.; Bhattacharya, S.; Sarkar, S.; Le Pera, E. Authigenic Green Mica in Interflow Horizons within Late Cretaceous Deccan Volcanic Province, India and Its Genetic Implications. *Minerals* **2022**, *12*, 198. https://doi.org/10.3390/min12020198

Academic Editor: Manuel Pozo Rodríguez

Received: 7 January 2022
Accepted: 31 January 2022
Published: 3 February 2022

1. Introduction

Fe- and K-bearing green authigenic mica, i.e., celadonite, has been observed in close association with basic igneous rocks [1–6]. Celadonite formation predominates hydrothermally altered mafic volcanics as infillings in fractures, veins, or vesicles [6–11]. However, it is also reported in volcano sedimentary rocks with a significant volcanogenic or tuffaceous input [12–15]. Syngenetic precipitation of green mica has been reported in several ore deposits, and its presence has been used as a tool to investigate the volcanogenic input and age of mineralization [14,16]. The Fe-bearing authigenic green mica has a significant role in paleoenvironmental characterization [17,18]. Celadonite commonly occurs in marine settings. Although the Fe_2O_3 content is mostly derived from mafic volcanics, the source of K_2O content in celadonite is debatable [5,14]. The K content of the submarine celadonite is derived from the seawater [3–9]. The formation of celadonite in a nonmarine environment

requires an alternate source of K [5,14,15,17–20]. The compositional variation of green silicates formed by the alteration of mafic volcanics reflects the availability of essential chemical constituents, the temperature of formation, redox conditions, and diagenetic alteration (e.g., [21]). Chemical and mineralogical characterization of the authigenic green silicates is necessary to infer their origin. Green silicates including celadonite, glauconite, chlorite, and illite have been detected on Mars, especially in the Gale Crater, based on their spectral signatures [22–28]. Therefore, the spectral signatures of authigenic green silicates are crucial for understanding the mineralogy of extraterrestrial clays.

Several studies have highlighted the occurrences of authigenic clay-rich red interbasaltic layers (i.e., red bole) within a continental flood basalt province. Red bole mainly contains smectite along with hematite [29–39]. However, very few cases discussed the origin of an authigenic green silicate-rich layer within volcanic rocks. The green clay-rich interbasaltic horizons between lava flows in the Late Cretaceous Deccan volcanic province in India are known as green boles [23,32,40,41]. Green boles are relatively less common than authigenic clay-rich red interbasaltic layers (known as red boles). Green boles occur locally as a lenticular bed a few centimeters to a meter thick and as centimeter-scale cavity-filling deposits. VNIR spectra revealed the presence of nontronite and celadonite in green boles (e.g., [23]). Several studies have provided geochemical characteristics of green boles [23,32,40,41], but petrographic details are not yet available. However, factors controlling the formation of interbasaltic green bole beds and the source of potassium for the formation of authigenic celadonite are still a topic of discussion. This study aimed to understand the origin of authigenic green silicates within the green bole beds of the Deccan volcanic province based on textural, chemical, and mineralogical characteristics.

2. Geological Background and Field Evidence

The Late Cretaceous Deccan Volcanic Province is one of the largest mafic continental flood basalt provinces of the world, formed during a time interval of 69 to 63 Ma, extending over hundreds of kilometers across western and central India, with a present-day areal extent of ~0.5 × 10^6 km^2 (e.g., [42–47]). It includes interbasaltic clay horizons several centimeters to a few meters thick formed by the alteration of basalt and tuffaceous/volcaniclastic units. These interbasaltic bole horizons are extensively reported in western India [33,36,39,48,49]. The Western Deccan volcanic province has been classified into three major subgroups based on variation in the geochemical regime: the Kalsubai (~2000 m), Lonavala (~525 m), and Wai (~1100 m) subgroups, which are further divided into 12 stratigraphic units [50–52]. The Late Cretaceous Salher green bole is relatively older, and it belongs to the Kalsubai subgroup, whereas the Pune green bole belongs to the Wai subgroup.

A detailed investigation was undertaken on green boles exposed in two sections, Salher (20°44′19.14″ N, 73°56′32.34″ E) and Pune (18°30′28.36″ N, 73°47′2.64″ E), Maharashtra, India (Figure 1). Green boles in Salher occur as 35 cm thick isolated pockets and lenses with ~2 m lateral extent at an elevation of 915 m above mean sea level (Figure 2A). They overlie the weathered flow top of the Deccan basalt. The flow top is highly altered, with secondary white and green minerals as vesicle fillings. The lava flow in Salher is dominated by compound lava flows. The upper contact of the green bole is sharp with the overlying basalt. Its lower contact is sharp, mostly convex downward, but irregular in places where it extends into the fractures on the underlying flow top (Figure 2A,B). The middle part of the green bole is homogeneous, showing distinct planar lamination. Three samples were collected from this location, including the fracture filling at the base of section (1), middle (2), and upper part (3) (Figure 2B). All the samples included green and white vug filling minerals. The green bole bed in Pune occurs as an approximately 30 cm thick lens, at a 610 m elevation above the mean sea level. It occurs above the fragmentary flow top and exhibits gradational lower and sharp upper contacts with the basalt (Figure 2C,D). Two samples were collected from this section.

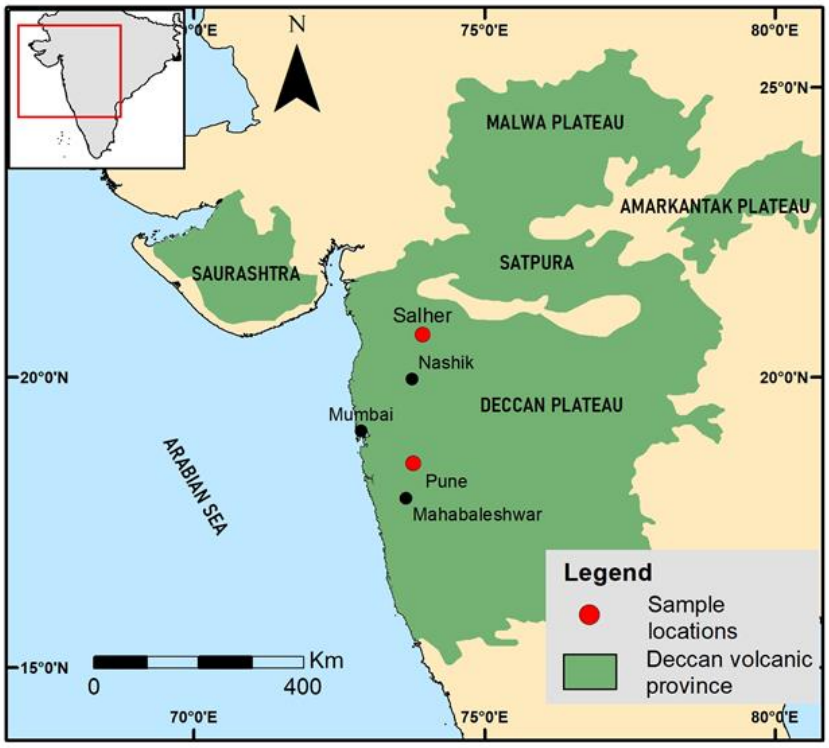

Figure 1. Map showing outcrop of Deccan volcanic province, India, and sampling locations marked by solid red circles (modified after Kale et al. [47]).

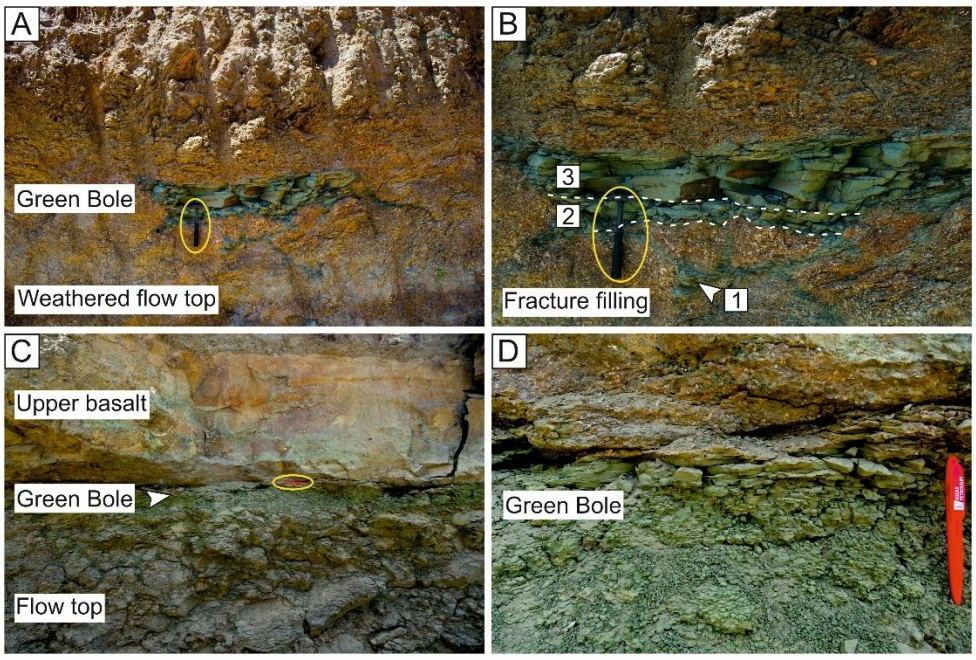

Figure 2. Field photographs showing: (**A**) isolated pocket of laminated green bole in Salher with maximum thickness up to 35 cm, lying above the weathered flow top. Note the sharp upper contact in Salher section, Nashik, Maharashtra; (**B**) close-up view of green bole in image (**A**) showing lamination, and with green bole sample positions marked as 1, 2, and 3; (**C**) green bole at Pune sharply overlain by basalt; (**D**) close-up view of the green bole in image C (hammer length = 38 cm, pen length = 14.5 cm). Scales in Figures (**A**–**C**) are highlighted with a yellow circle.

3. Methods

Soft and friable samples were impregnated with a 1:1 mixture of East Coast Resin© (epoxy resin and hardener) before cutting and grinding for petrographic investigation under an optical microscope. The impregnated samples were kept in a hot-air oven at 50 °C overnight for hardening. The hardened samples were cut, ground, and polished using silicon carbide paper. The polished surface was mounted on a glass slide using a 2:1 mixture of cold setting Buehler© EpoThin^{TM} 2 epoxy resin and Buehler© EpoThin^{TM} 2 epoxy hardener. A Buehler© PetroThin sectioning system was used to cut the mounted samples. Thin sections were examined using a Leica DM 4500P polarizing microscope. Images were taken with a Leica DFC420 camera and processed using Leica Image Analysis software (LAS- v4.6). For clay mineralogy, XRD analysis was carried out using Cu Kα radiation (45 kV, 40 mA) and a nickel filter in an Empyrean X-ray diffractometer with a Pixel 3D detector at the Department of Earth Sciences, Indian Institute of Technology Bombay. Rock samples were powdered using an agate mortar and pestle. The <2 μm clay size fraction was separated by centrifugation after suspension and sedimentation of coarse nonclay fractions in Milli-Q water (18 MΩ) column [53,54]. Random preparations were made on a zero-background Si sample holder using <2 μm clay separate and scanned for 4 to 70° 2θ, with a scan speed of 43 s/step and a step size of 0.013° 2θ. Additionally, slow scans were performed in the region of 59 to 63° 2θ (0.013° 2θ step size and 148 s scan step time) to characterize 060 reflections of the clay minerals. An oriented clay mount of <2 μm clay size fraction was prepared on glass slides [54]. The oriented mounts were scanned from 4 to 30° 2θ with a 0.013° 2θ step size for qualitative analysis of clay minerals. They were analyzed each time after drying, glycolation (with ethylene glycol), and heating at 400 °C and 550 °C, using the same instrumental settings [55]. Qualitative identification of mineral phases was carried out using Panalytical© HighScore™ software. All three samples of Salher and two samples of Pune green bole were analyzed under XRD. XRD patterns of one sample each from the Salher (SL) and Pune (PN) green boles are presented in this paper due to their similarity in mineralogical composition. For morphological investigation, fresh rock chips of 5 mm × 2 mm dimension were mounted on the stub, and a platinum coating (15 nm) was applied on the sample with a sputter coater to avoid charging. The samples were analyzed under a JEOL JSM-7600F FEG–SEM at the Sophisticated Analytical Instrument Facility, Indian Institute of Technology Bombay.

Visible near-infrared (VNIR) spectroscopy of the three powdered samples from Salher (SL-1, 2, and 3) and one powdered sample from Pune (PN) was carried out using a FieldSpec® 4 high-resolution spectroradiometer (Analytical Spectral Devices, Boulder, CO, USA) at the Space Applications Centre, Indian Space Research Organization, Ahmedabad. The reflectance spectra of the green bole were collected under laboratory conditions over a wavelength range of 0.35–2.5 μm (VNIR range), using a contact probe attached with the FieldSpec® 4 high-resolution instrument. The contact probe was equipped with a high-intensity light source; i.e., a 100 W halogen reflectorized lamp, with a fiber-optic input socket. For better results, a 30° angle was maintained between the halogen lamp and the fiber-optic input socket. Details of methodologies are provided in Bhattacharya et al. [56] and Naveen et al. [57]. The IR absorption spectra of <2 μm clay were recorded with a Bruker Vertex 80 FTIR system at the Sophisticated Analytical Instrument Facility, Indian Institute of Technology Bombay. For each sample, 256 scans were recorded (on the Bruker spectrometer) in the MIR region (400–4000 cm^{-1}) with a resolution of 4 cm^{-1}. The IR absorbance conversion was made automatically with the OPUS 8.2.28 software package (Bruker Ltd., Billerica, MA, USA). All the samples were prepared using the KBr pressed-disc technique. To make a KBr pellet, 0.5 mg of sample was dispersed in 200 mg of KBr, and the resulting mixture was placed in a 13 mm pellet die and pressed under room temperature. The pellet was then placed into a glass desiccant box with $CaCl_2$ and heated in a furnace at 110 °C for 24 h. The peak deconvolution in the selected area of the OH-stretching region was done using OriginPro 2019b software. VNIR and FTIR spectroscopy were done for detailed characterization of clay minerals.

Mineral chemical investigations of different phases within the green boles were carried out using a Cameca SX 5 electron probe microanalyzer (EPMA) with an accelerating voltage of 15 kV, a specimen current of 20 nA, and a nominal beam diameter of 1 µm (peak: 10–20 s and background counting: 5–10 s) at the Department of Earth Sciences, Indian Institute of Technology Bombay. Minerals and synthetic phases were used as laboratory standards for the calibration of the EPMA data. Duplicate analysis of individual points shows an analytical error of less than 1%. All data points on the mineral of interest were selected using a combination of optical and backscattered electron image control. The EPMA data were ZAF corrected.

4. Results

4.1. Petrographic and Morphological Description

Petrographic analysis of the green bole bed in Salher revealed volcanic lithic fragments, green authigenic clay, plagioclase, and vesicular volcanic glasses (up to 200 µm) as primary constituents (Figure 3A).

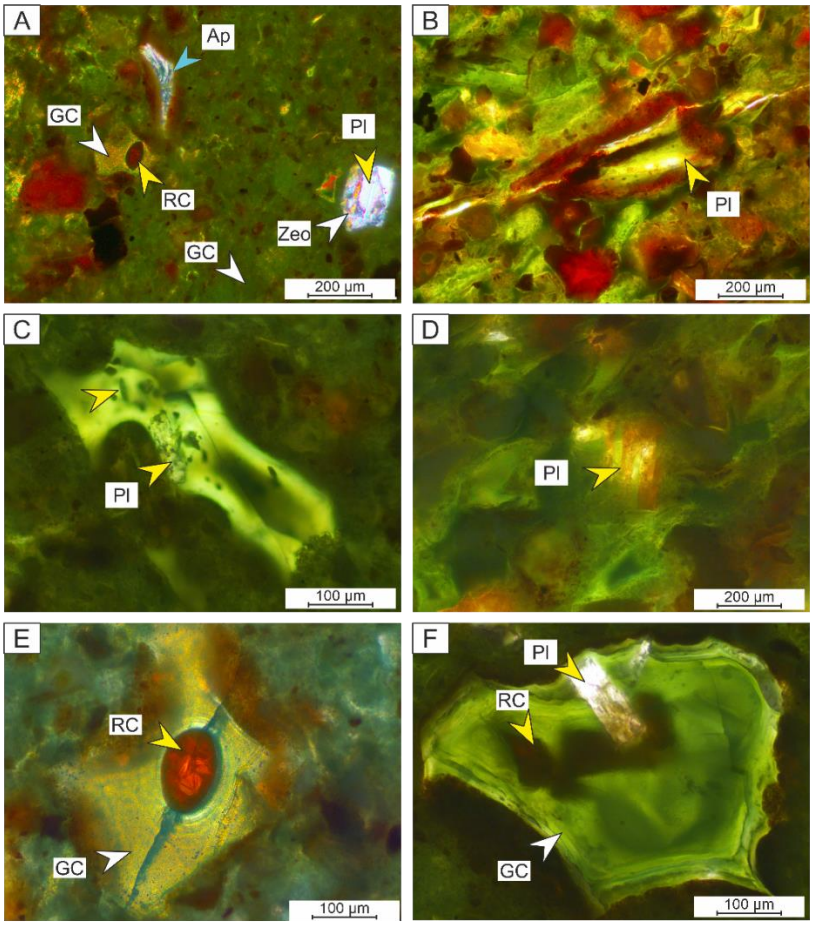

Figure 3. Photomicrographs of samples from the green bole in Salher (**A**) Fine-grained green groundmass (GC; white arrow) with zeolite (Zeo; white arrow) replacing plagioclase (Pl; yellow arrow) around the rim, and green clay replacing glass shard (GC; white arrow) under plane-polarized light. Note that vesicles of replaced glass shards are filled with red clay (RC, yellow arrow). Sickle-shaped apatite (Ap; blue arrow) grain also occurs as a minor constituent; (**B**) Plagioclase (Pl; yellow arrow) replaced by green clay under plane-polarized light; (**C**,**D**) Relics of plagioclase (Pl; yellow arrow) laths surrounded by green clay under plane polar light; (**E**) Glass shard replaced by green clay (GC; white arrow). Note red clay (RC; yellow arrow) precipitate within the pore; (**F**) Green clay (GC; white arrow) grain along with red clay (RC; yellow arrow) and plagioclase lath (Pl; yellow arrow) (under plane-polarized light).

It also included mud clasts (up to 2 mm long), subrounded fine-grained green clasts (up to 500 µm), and highly altered basalt clasts with plagioclase laths (up to 100 µm). Pyroxene, apatite, and opaques occurred as minor constituents (Figure 3A). Authigenic green minerals occurred as replacing plagioclase (Figure 3B–D) and glassy phase within volcanic lithic fragments (Figure 3E,F). It also occurred as fine precipitates within groundmass (Figure 3A,E) and glass vesicles (Figure 4B–D). Red clay minerals occurred as the replacement of basaltic fragments, as precipitate within intergranular pore spaces (Figure 4A), and glass vesicles (Figure 4B–D). In places, the red phases precipitated at the center of vesicles after the formation of green minerals (Figure 4B–D). The vesicles within the volcanic glasses were often oversized (Figure 4C,D). Authigenic zeolite occurred as alteration of plagioclase (Figure 3A), microscale veins intersecting grains (Figure 3B), and within oversized voids (Figure 4C,D).

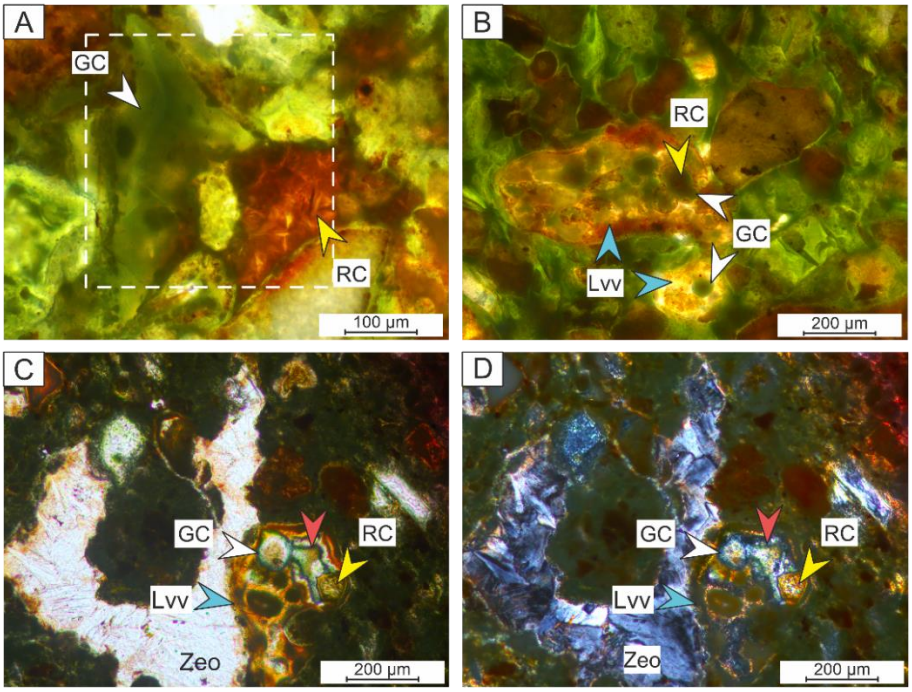

Figure 4. Photomicrographs of samples from the Salher green bole (**A**) Red clay (RC; yellow arrow) and green clay (GC; white arrow) under plane-polarized light; (**B**) Green clay (GC; white arrow) within vesicles of altered glass (Lvv; blue arrow). Note red clay (RC; yellow arrow) at the center of vesicle; (**C**) Fibrous zeolite (Zeo) occurring as void filling. Note that glass (Lvv; blue arrow) is completely altered/palagonized, and vesicles are enlarged (red arrow; under polar plane light). Green clay (GC; white arrow) occurs within enlarged vesicles (red arrow) of glass as film. Note the red clay toward the center (RC; yellow arrow) of vesicle; (**D**) Cross polar image of (**C**).

The green bole in Pune showed lithic and vitric grains of different sizes within fine-grained groundmass. The long dimension of basalt clasts ranged from 500 µm to 2.5 mm, which included plagioclase laths, altering into yellow and green clay minerals (Figure 5A). Olivine and pyroxene within basaltic clasts were mostly replaced by iron oxide and clay minerals, with a few relicts of original minerals (Figure 5A). Plagioclase (Figure 5B,C) and pyroxene (Figure 5B) phenocrysts were variably altered to green clay minerals. Few pyroxene grains showed saw-edge-like dissolution features (Figure 5E,F). Green clays also occurred as films around intergranular pores filled with zeolite (Figure 5A) and as altered glasses (Figure 5D). Some glass shards were altered to yellow clay minerals (Figure 5D). Opaque phases were abundant within altered basaltic fragments and the matrix (Figure 5A–C). Under the scanning electron microscope, the elongated lathlike morphology (less than 1 µm) (Figure 6A) corresponded to green clay, and the honeycomb morphology corresponded to smectite (Figure 6B).

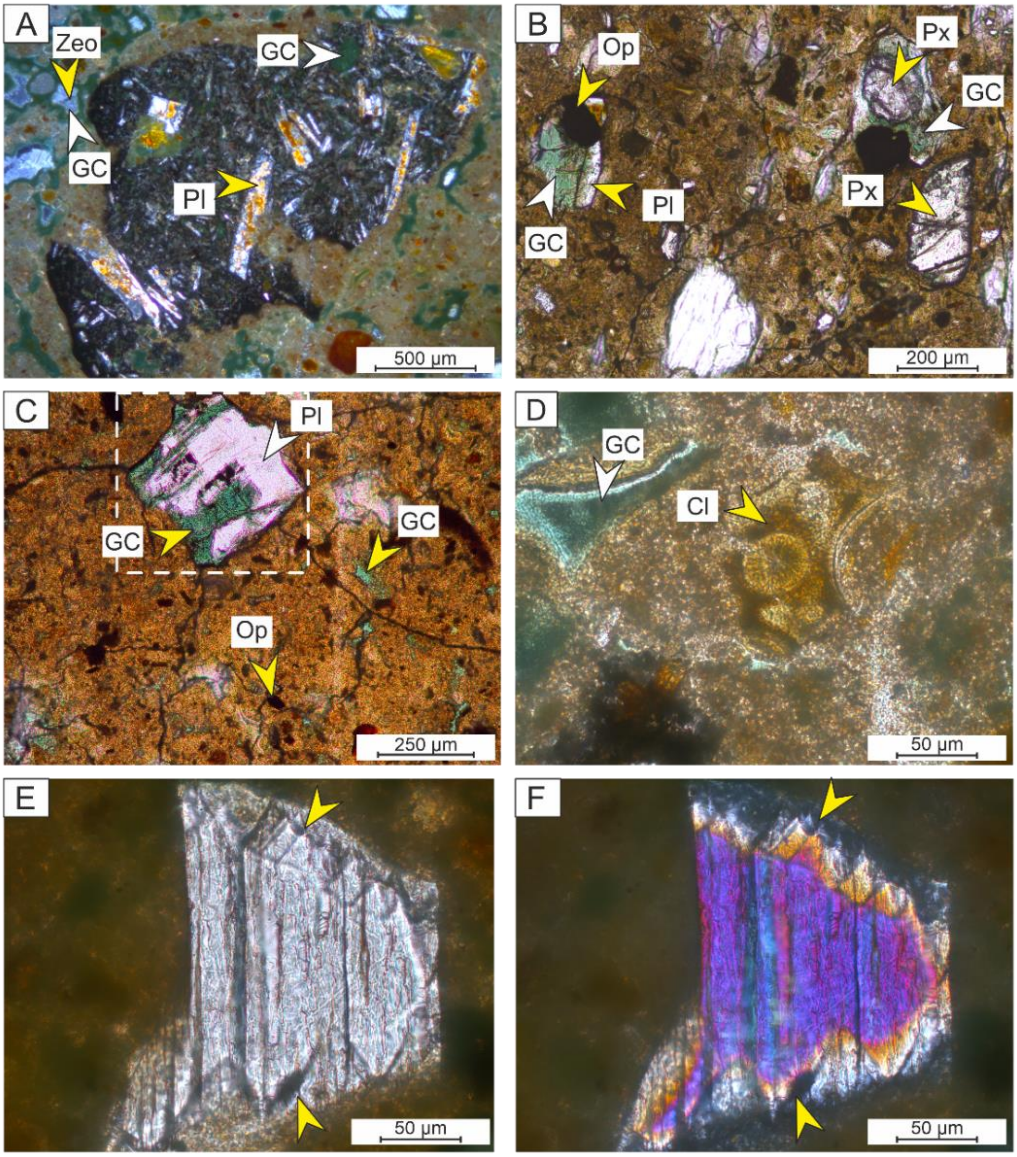

Figure 5. Photomicrographs of samples from the Pune green bole (**A**) Basaltic fragment, with sericitized plagioclase laths (Pl; yellow arrow) and green clay (GC; white arrow) lining voids and pores, followed by zeolite (yellow arrow) (under cross-polar light); (**B**) Plagioclase (Pl; yellow arrow), pyroxene (Px; yellow arrow), and opaques (Op; yellow arrow) present in a fine-grained groundmass of the green bole. Plagioclase (Pl) and pyroxene (Px) alter into green clay (GC; white arrow); (**C**) plagioclase (Pl; white arrow) altering into green clay mineral (GC; yellow arrow) along cleavages and fractures. Green clay also occurs in groundmass as replacing the interstitial glass; (**D**) Green clay (GC; white arrow) occurring as void filling, and glass shard completely replaced by clay mineral (Cl; yellow arrow); (**E**) Saw-edge-like dissolution feature (yellow arrow) in pyroxene under plane-polarized light; (**F**) Cross-polar image of (**E**).

4.2. X-ray Powder Diffraction and Unit-Cell Parameters

The XRD patterns random preparation of <2 µm clay samples from the Salher and Pune green boles revealed different mineral phases, based on characteristic hkl reflections (Figure 7). The XRD patterns of the oriented clay mount showed strong reflection at ~10 Å and ~15 Å under air-dried conditions. After glycolation, the ~10 Å peak remained unmoved, but the ~15 Å peak shifted to ~16.90 Å in both samples, which collapsed to ~10 Å upon heating at 400 °C and 550 °C for 90 min (Figure 8). The characteristic 001 peak at

10 Å, sharp hkl reflection with distinct 002 and 023 peaks, relatively prominent $11\bar{1}$ and 021 reflections, splitting up of $13\bar{1}$ and 130, and <1.510 Å d060 reflections indicated the presence of celadonite [1–3,11,14,58–60]. In addition, the 003 and 022 peaks were split up in celadonite (Figure 7) [59,60]. The relatively higher intensity of the 022 peak could have been due to the presence of quartz.

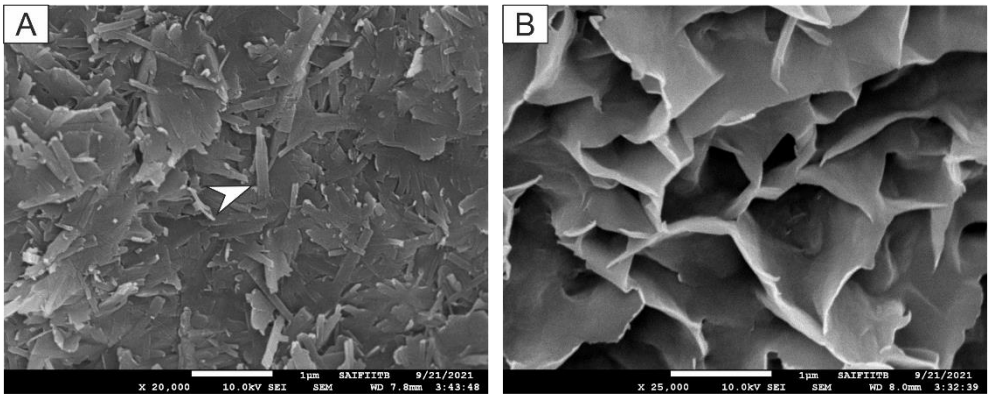

Figure 6. SEM images of: (**A**) elongated lathlike morphology of green clay (white arrow); (**B**) honeycomb morphology, typical of smectite.

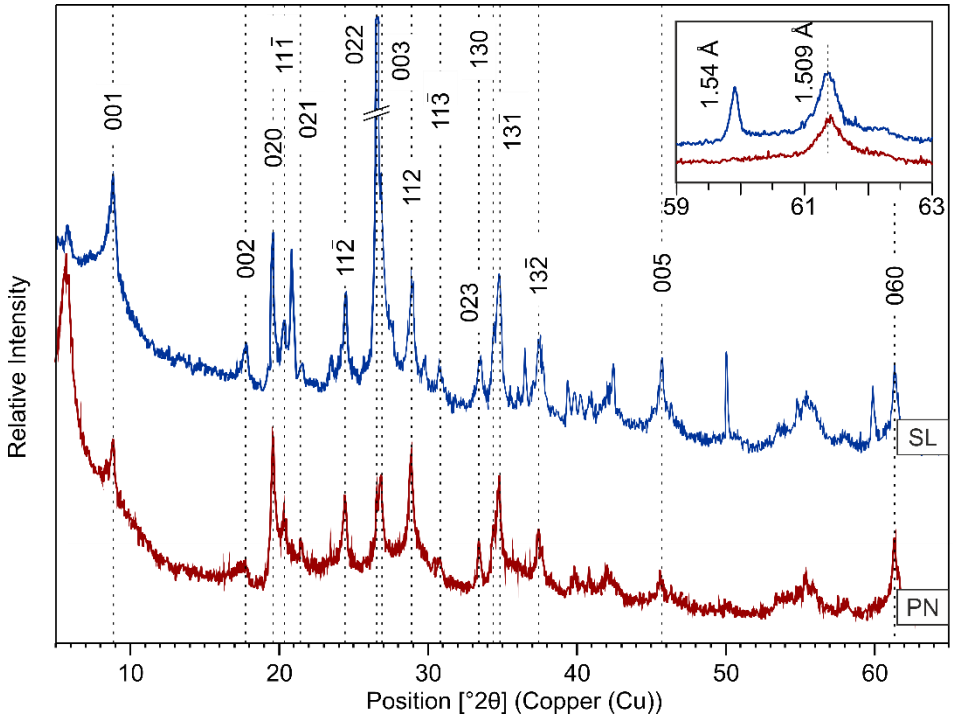

Figure 7. Powder XRD pattern of random mounts of <2 µm clay size fraction. The blue and red lines indicate XRD reflections of samples from the green boles in Salher (SL) and Pune (PN), respectively. Vertical dotted lines show characteristic reflections of celadonite. XRD pattern in upper right corner indicates slow scan between 59° and 63° 2θ.

The XRD peaks of celadonite were in good agreement with the results obtained in previous studies [1,2,7,13,14]. The ~3.63 Å and ~3.08 Å peaks corresponding to $11\bar{2}$ and 112, respectively, reflected a well-ordered 1 M mica polymorph [1,3,7,13,61]. The value of d060 spacing of the studied green phyllosilicate (~1.509 Å) was close to the data (between 1.507–1.509 Å) formerly reported in the literature for dioctahedral mica; i.e., celadonite [2,5,14]. The low-intensity d002 peak of celadonite suggested destructive

interference (Figures 7 and 8) related to the high octahedral Fe content [2,62]. The shift of ~15 Å peak (under air-dried conditions) on glycolation and its collapse upon heating confirmed the presence of smectite (Figure 8). The relatively broad reflection near 1.50 Å indicated the overlapping of 060 reflections of dioctahedral smectite and celadonite [3,21]. The presence of quartz in the Salher green bole was identified by 4.27 Å, ~3.34 Å, 2.46 Å, 2.28 Å, 1.98 Å, and 1.82 Å peaks (Figure 7). Therefore, the X-ray powder diffraction patterns of the <2 μm clay separated fraction of the green boles showed the presence of celadonite, smectite, and quartz.

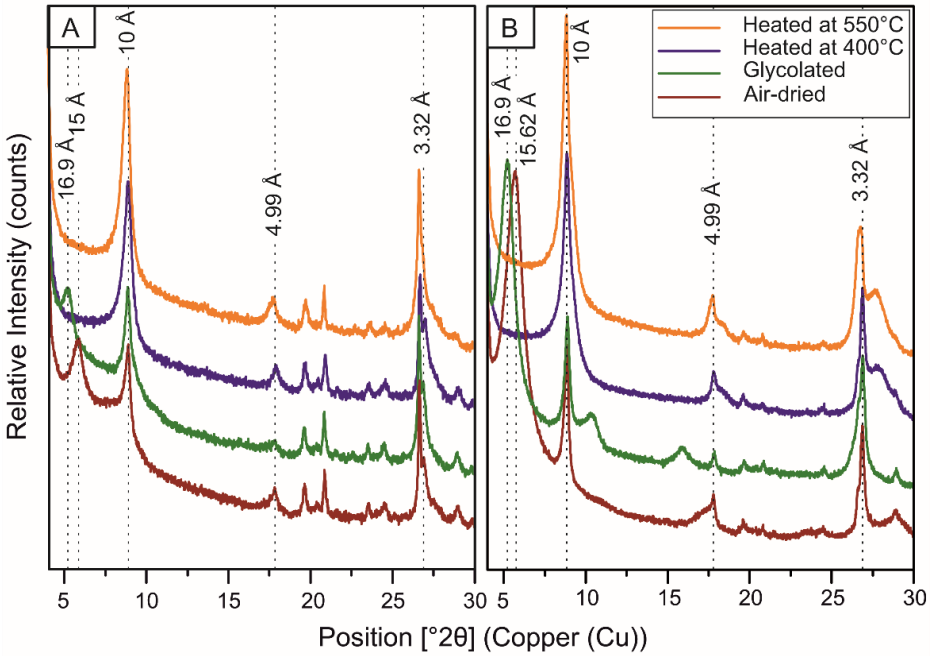

Figure 8. XRD pattern of oriented clay mount (air-dried, solvated with ethylene glycol, and heated at 400 °C and 550 °C for 90 min each) of green bole samples from Salher (**A**) and Pune (**B**).

The determination of the unit cell parameters, i.e., a, b, c, and β of the authigenic green mica structure, was carried out using experimental d(hkl) values. The b and a parameters of the structure were assumed to be 6 × d(060) and b/$\sqrt{3}$, respectively [63,64]. The unit cell parameters c and β were calculated from the d values of the 112 and $11\bar{2}$ reflections (3.0879 Å and 3.6361 Å for SL; 3.08523 Å and 3.6305 Å for PN) using the formulae given in the paper by Sakharov et al. [64] (Table 1). The unit-cell parameters of the studied samples occurred within the ranges provided for celadonite in the literature [59,63], which corroborated the identification of the green authigenic minerals as celadonite.

Table 1. Unit-cell parameters of the studied authigenic green mineral (celadonite).

Sample	Unit-Cell Parameters					
	a (Å)	**b (Å)**	**c (Å)**	**β °**	**csinβ (Å)**	**ccosβ/a**
SL	5.2275	9.0542	10.156	100.685	9.9801	−0.3602
PN	5.2259	9.0516	10.1318	100.45	9.9636	−0.3516

4.3. Visible Near-Infrared Spectroscopy

Spectra of samples from the Salher green bole showed weak bands near 0.41 μm, 0.45 μm and ~0.50 μm; broad and shallow absorption bands near ~0.74 μm, ~0.94 μm, and 1.085 μm; a shallow asymmetrical absorption band at 1.41 μm; a sharp and deep asymmetrical band near 1.91 μm; and shallow peaks between 2.20 and 2.50 μm (Figure 9).

The green bole of Pune showed similar reflectance spectra as well as more prominent ~0.50 µm, 1.41 µm, and 2.21 µm absorption bands compared to the Salher green bole.

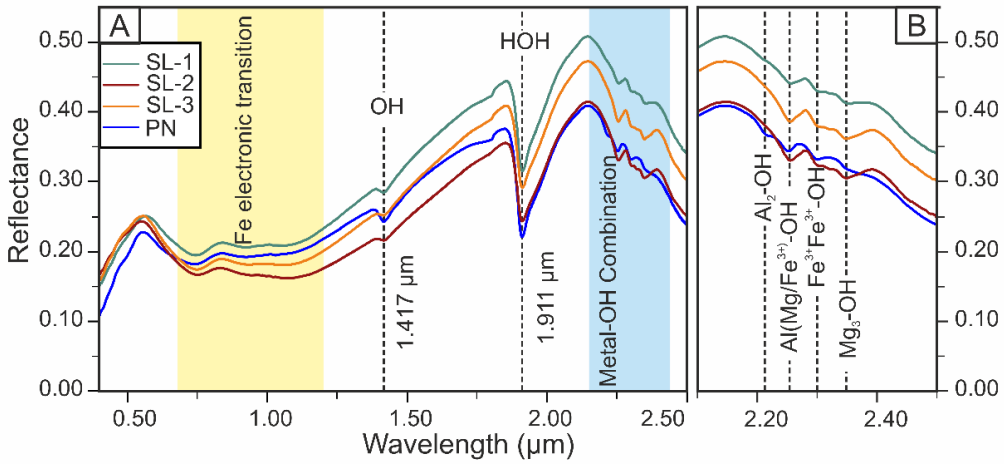

Figure 9. (**A**) VNIR reflectance spectra of the green bole samples from Salher (SL-1, 2, 3) and Pune (PN); (**B**) enlarged image of the metal–OH combination band (2.00–2.50 µm).

The reflectance spectra of the green bole samples revealed weak absorption features in the extended visible region, i.e., 0.40–1.10 µm due to crystal-field and charge-transfer effects in iron-bearing minerals, viz. celadonite and smectite [22,65]. The absorption features between 1.40 and 2.50 µm suggested a combination and overtones of the H–O–H bound to interlayer regions or absorbed on the mineral surface, and the OH bound to octahedral cations [66–69]. A relatively shallow absorption band center at ~1.40 µm and a sharp and deep band at ~1.90 µm with shoulders on the right of both bands indicated an OH stretching overtone and H_2O combination, respectively. This overtone band depended on cation at the octahedral position; i.e., at 1.43 µm for Fe_2–OH [68–71], 1.41 µm for Al_2–OH [68–70], and 1.38–1.39 µm for Mg_3–OH [66–72]. The depth of the absorption band center at ~1.9 µm corresponded to the amount of H_2O content in the interlayers of clay minerals, extra-framework sites of zeolite, and surface hydration.

Metal–OH combination bands between 2.20–2.50 µm depend on the relative proportion of Fe, Mg, and Al cations in the octahedral position of phyllosilicate [66–68]. Characteristic absorptions of approximately equal strengths at ~2.30 µm ($Fe^{3+}Fe^{3+}$–OH combination) and 2.35 µm (Mg_3–OH combination) and a strong slope between 1.00 µm and ~2.10 µm confirmed the presence of celadonite (Figure 9). A weak absorption band center near 2.25 µm indicated an Al(Mg/Fe^{3+})–OH combination in the celadonite [22,23,69,73]. The relatively strong band near 2.25 µm suggested the co-occurrence of celadonite and smectite. The absorption features around 2.21 µm inferred the Al_2–OH combination band (stretching and bending vibrations). A doublet feature near 2.21 µm and 2.25 µm and a slight shift of the 1.40 µm band toward the higher reflectance revealed the presence of an additional component (Fe_2–OH combination) mixed with the Al-phyllosilicate [22,41,66,74]. The Fe^{3+} electronic excitations near 0.95 µm, OH stretching overtone bands near 1.417 µm (AlFe^{3+}–OH combination), and the OH stretching and bending combination bands (OHν + δ) observed near 2.29 µm suggested a composition of smectite between Fe-montmorillonite and nontronite [65–71,74–80].

4.4. Fourier-Transform Infrared Spectroscopy

The FTIR spectra of <2 µm clay were analyzed for specific regions: Si–O bending (600–400 cm^{-1}), Si–O stretching and OH-bending (1200–700 cm^{-1}), and OH-stretching (3700–3500 cm^{-1}) positions. In the Si–O bending region, the prominent bands were ~439 cm^{-1}, ~460 cm^{-1}, and ~500 cm^{-1}. The Si–O stretching region showed absorption bands near 977–979 cm^{-1}, 1080 cm^{-1}, and ~1114 cm^{-1}. The OH-bending mode showed

absorption bands near ~800 cm^{-1} and ~865 cm^{-1} (Figure 10B). The OH-stretching region showed three sharp bands between 3550 and 3650 cm^{-1} and a broad band near 3400 cm^{-1} (Figure 10A). The absorption bands in the FTIR spectra were assigned a specific vibration mode based on interpretations from previous literature [1,14,59,79–81].

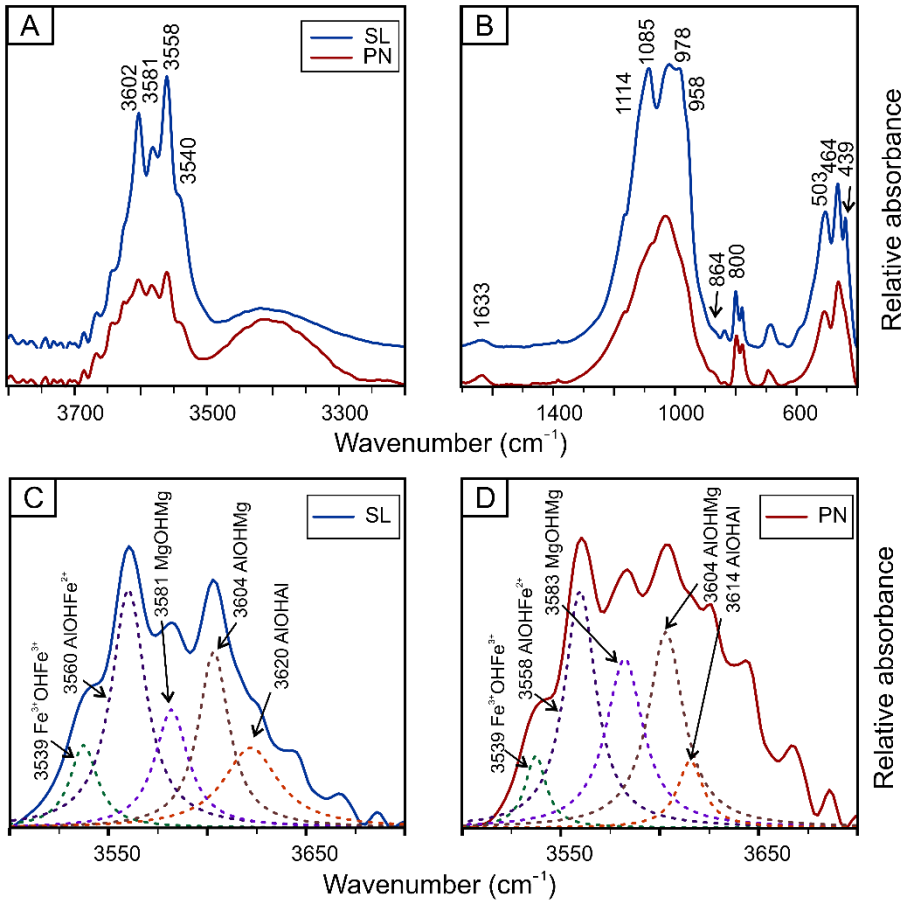

Figure 10. (**A**,**B**) FTIR absorbance spectra of the green bole samples from Salher (SL) and Pune (PN); decomposition and curve-fitting of the FTIR spectra of samples from (**C**) Salher (SL) and (**D**) Pune (PN) in the OH-stretching region.

The spectra of studied samples showed three sharp bands in Si–O bending vibration mode. The three sharp bands; i.e., ~439 cm^{-1}, ~464 cm^{-1}, and 503–509 cm^{-1}, corresponded to Si–O (δ1), Si–O–Si (δ2), and Si–O–M (δ3) (M indicates octahedral Al or Fe), respectively, which is typical in spectra of all dioctahedral mica. In the Si–O stretching region, four prominent peaks occurred, with the strongest peak between 950 cm^{-1} and 1110 cm^{-1}. The presence of two sharp, well-resolved bands at 978 cm^{-1}, 1085 cm^{-1} and the shoulder at 958 cm^{-1}, 1114 cm^{-1} inferred the presence of celadonite. These bands are ascribed to vibrations within the tetrahedral sheet [59,79–83]. The peaks on the lower wavenumber side of the Si–O stretching region corresponded to the bending of OH bounded to octahedral cations. The distinct absorption bands at ~800 cm^{-1} and ~865 cm^{-1} were assigned to (Fe(III)OHMg) and (AlOHFe(III)) vibrations of celadonite, respectively. The band near 1633 cm^{-1} indicated the presence of water inside the silicate layers (Figure 10B) (e.g., [81]).

In the OH-stretching region, the positions and intensities of the absorption bands depended on the cation distribution in the octahedral sheet. A sharp band at 3558–3560 cm^{-1} (Fe(III)OHMg or AlOHFe(II), 3581–3583 cm^{-1} (MgOHMg), 3604 cm^{-1} (AlOHMg), and a shoulder near 3539 cm^{-1} (Fe(III)OHFe(III) confirmed the presence of celadonite (Figure 10C,D) [5,81–83]. In addition, AlOHAl (3615–3620 cm^{-1}) was determined by spectrum decomposition and curve-fitting. The wide OH-stretching band between 3400 cm^{-1} and 3500 cm^{-1} corresponded to adsorbed H_2O [3].

4.5. Mineral Chemistry

The EPMA data revealed considerable variation in major element compositions among the green celadonite minerals from the Salher and Pune green boles (Table 2). The K_2O content of Salher celadonite varied from 7.90 to 8.97 wt %, Fe_2O_3 from 14.20 to 17.15 wt %, MgO from 4.10 to 5.33 wt %, SiO_2 from 53.95 to 57.79 wt %, and Al_2O_3 from 9.25 to 12.28 wt %. (Table 2). The subrounded brown-orange vesicular glasses (Figure 4B–D) exhibited high SiO_2 ranging from 56.49 to 66.24 wt %, Al_2O_3 ranging from 14.69 to 17.75 wt %, K_2O between 11.98 and 14.68 wt %, and Fe_2O_3 (total) less than 1.00 wt %. The red clayphase was iron-rich, with SiO_2 ranging from 41.01 to 51.19 wt %, Al_2O_3 from 10.84 to 18.19 wt %, Fe_2O_3 (total) from 16.92 to 23.59 wt %, MgO from 6.53 to 12.46 wt %, and CaO less than 3.00 wt %. The chemistry of the red phase indicated Fe-smectite (Figures 3E,F and 4A,B). The Na_2O content of plagioclase grains varied from 3.99 to 11.51 wt %. The zeolite was Ca-rich, with SiO_2 ranging from 58.66 to 72.59 wt %, Al_2O_3 ranging from 11.11 to 16.82 wt %, and CaO varying from 4.85 to 7.80 wt %. The plagioclase composition was consistent with labradorite-bytownite and albite (av. albite). The authigenic zeolites belonged to the Ca-rich variety, similar to heulandite. X-ray mapping revealed higher contents of Si and K (Figure 11B,C) and lower contents of Fe and Mg of the celadonite than in the associated red clay (Figure 11D,E).

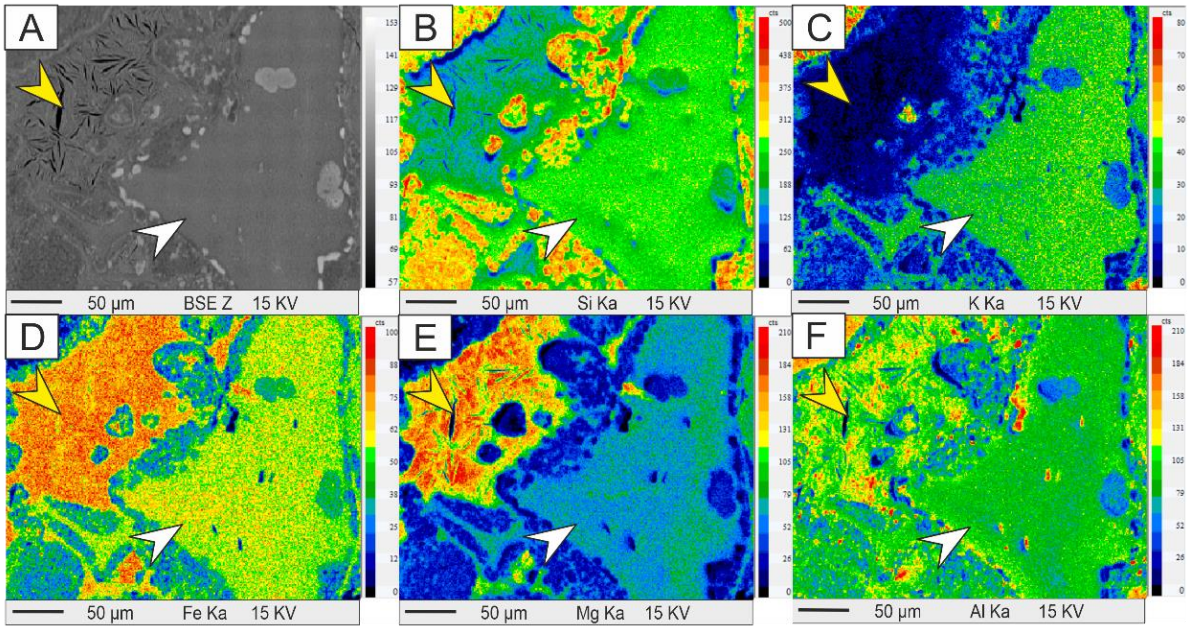

Figure 11. (**A**) EPMA backscatter image showing elemental mapping of a portion of green and red clay (marked by rectangular box in Figure 4A) showing Fe-rich smectite (yellow arrow) and celadonite (white arrow). X-ray mappings show abundances of Si (**B**) and K (**C**) in celadonite and dominance of Fe (**D**) and Mg (**E**) in Fe-smectite. Fe-Smectite show slightly higher Al content than celadonite (**F**).

Green authigenic clay; i.e., celadonite, within the Pune green bole showed a negligible variation in mineral chemistry (Table 2). The celadonite showed a range of K_2O from 8.83 to 9.76 wt %, Al_2O_3 from 5.13 to 6.98 wt %, MgO from 4.37 to 5.97 wt %, and Fe_2O_3 (total) from 16.11 to 19.53 wt %. The Fe-smectite clay showed SiO_2 ranging from 41.04 to 45.52 wt %, Al_2O_3 from 10.86 to 12.00 wt %, Fe_2O_3 (total) from 21.61 to 24.98 wt %, MgO from 9.07 to 14.13 wt %, and CaO less than 5 wt %. X-ray mapping showed the alteration of plagioclase into celadonite along cleavage and weak planes in green bole samples from Pune (Figure 12).

Table 2. Concentrations of major oxides (wt %) in celadonite studied in Pune and Salher green boles.

Sr. No.	SiO_2	Al_2O_3	Fe_2O_3 (Total)	MgO	MnO	TiO_2	CaO	K_2O	Na_2O	Total
Pune										
1	55.67	5.35	19.01	5.52	0.01	0.02	0.26	9.48	0.09	95.41
2	55.16	5.24	19.06	5.57	0.01	0.12	0.16	9.52	0.04	94.88
3	55.99	5.44	19.14	5.40	0.01	0.00	0.11	9.68	0.06	95.84
4	56.24	5.13	19.43	5.70	0.01	0.06	0.15	9.76	0.07	96.55
5	51.93	6.98	17.21	5.70	0.03	0.38	0.2	9.15	0.11	91.71
6	53.38	6.49	16.84	5.97	0.02	0.37	0.15	9.23	0.04	92.48
7	51.64	5.79	16.11	5.56	0.00	0.35	0.14	9.25	0.04	88.87
8	50.09	5.28	17.49	5.03	0.00	0.35	0.12	9.62	0.06	88.03
9	56.16	5.73	19.00	5.80	0.06	0.04	0.22	9.37	0.11	96.5
10	55.50	5.35	19.47	5.53	0.00	0.09	0.18	9.44	0.12	95.69
11	56.18	5.32	19.53	5.69	0.03	0.10	0.17	9.47	0.08	96.55
12	53.69	5.73	19.34	5.03	0.04	0.28	0.37	8.83	0.12	93.42
13	55.04	5.91	19.01	5.73	0.06	0.04	0.31	9.04	0.13	95.26
14	50.76	5.25	19.40	4.37	0.02	0.1	0.31	9.20	0.10	89.51
15	55.96	5.78	19.40	5.83	0.04	0.07	0.24	9.28	0.07	96.66
16	54.55	6.16	15.22	5.55	0.00	0.44	0.28	8.84	0.08	91.11
17	54.41	5.57	16.59	5.31	0.00	0.37	0.12	9.05	0.04	91.46
18	53.00	6.64	17.71	5.92	0.01	0.30	0.09	9.16	0.07	92.88
Salher										
1	54.64	11.73	15.01	4.44	0.02	0.66	0.67	7.90	0.01	95.07
2	57.79	10.08	14.87	5.07	0.05	0.40	0.35	8.41	0.02	97.04
3	55.77	12.28	14.20	4.76	0.00	0.29	0.42	8.27	0.05	96.02
4	56.32	10.49	15.26	5.03	0.09	0.34	0.45	8.25	0.05	96.26
5	55.36	11.24	15.52	5.05	0.04	0.30	0.31	8.42	0.02	96.24
6	57.18	11.78	14.60	4.89	0.00	0.33	0.41	8.57	0.01	97.77
7	55.63	10.45	15.03	5.33	0.01	0.41	0.39	8.34	0.04	95.62
8	53.95	10.93	15.47	4.44	0.00	0.39	0.17	8.28	0.08	93.70
9	56.14	11.62	14.50	4.76	0.00	0.48	0.11	8.83	0.00	96.45
10	54.17	9.25	17.15	4.86	0.00	0.33	0.58	8.25	0.06	94.65
11	56.76	10.08	15.31	4.86	0.00	0.39	0.34	8.75	0.04	96.53
12	55.41	9.95	15.17	4.73	0.02	0.38	0.16	8.85	0.07	94.75
13	55.99	10.21	14.96	4.10	0.07	0.39	0.14	8.97	0.10	94.92
14	55.79	9.93	15.58	4.87	0.01	0.43	0.43	8.65	0.01	95.70
15	58.73	9.59	15.83	5.28	0.00	0.43	0.43	8.69	0.08	99.06
16	55.01	9.62	16.05	5.03	0.02	0.47	0.39	8.97	0.00	95.57

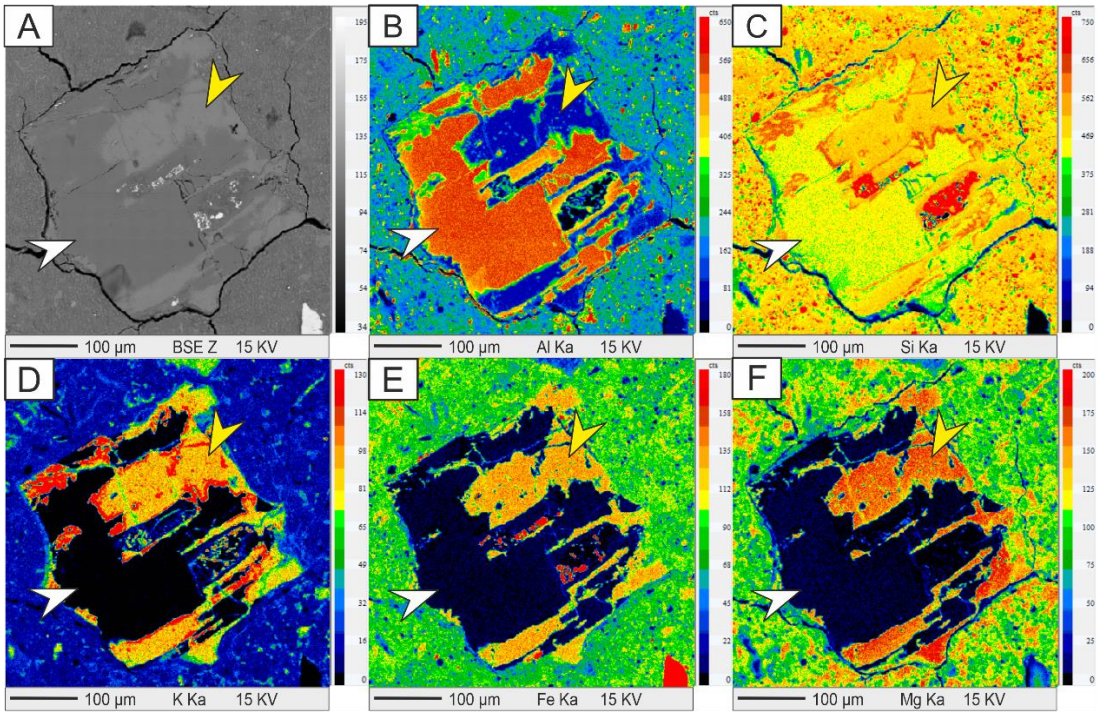

Figure 12. EPMA backscatter image (**A**) of plagioclase (marked by rectangular box marked in Figure 5C); X-ray elemental mappings show plagioclase (white arrow) altering along cleavage and weak planes into celadonite (yellow arrow) with loss of Al (**B**) and addition of Si (**C**) K (**D**), Fe (**E**), and Mg (**F**). Fe oxyhydroxide is recognized as white and red phases in (**A**) and (**E**), respectively.

All EPMA values were normalized to 100 wt % on an anhydrous basis to present the data in cross-plots. Celadonite data of Salher and Pune were compared with the published data reported from continental celadonite [5,14] using different symbols in Figure 13. The significant results of different cross-plots reveal the following significant aspects.

(a) A cross-plot of Al_2O_3 vs. Fe_2O_3 (total) showed two clusters for Salher and Pune celadonites. Salher celadonite showed higher Al_2O_3 and slightly lower Fe_2O_3 (total) contents than Pune celadonite (Figure 13A). The Al_2O_3 content, varying from 9.25 to 12.28 wt %, caused a scattering of data points for Salher.

(b) The K_2O vs. Fe_2O_3 (total) cross-plot formed two clusters for Salher and Pune celadonites (Figure 13B). Celadonites from Salher showed a lower content of K_2O, ranging from 7.90 to ~9.00 wt %. while those from Pune exhibited a consistently high content of K_2O (average 9.00 wt %).

(c) A K_2O vs. MgO plot showed lower content of MgO in the Salher celadonite (avg. 4.84 wt %) than Pune (avg. 5.51 wt %) celadonite (Figure 13C).

(d) A cross-plot between Si^{4+} and interlayer cations M^+ (i.e., K^+ Ca^{2+} Na^+) showed more than 3.85 Si^{4+} atoms per formula unit (pfu) in most celadonite data of Salher and Pune (Figure 13D). A few celadonites from Salher showed relatively lower content (3.77–3.89 atom pfu). The interlayer cation ranged from 0.75 to 0.82 atom pfu in celadonite from Salher, and from 0.85 to 0.96 atom pfu in celadonite from Pune.

(e) A cross-plot between octahedral (VI)Al^{3+} and interlayer cation (M^+) showed two clusters for the celadonite data of Salher and Pune (Figure 13E).

The structural formula of celadonite was calculated on the basis of four tetrahedral and two octahedral cations, and 22 positive charges [5,6], by the normalization of EPMA data to the dioctahedral mica formula (Table 3). The total Fe was considered as Fe^{3+}.

Table 3. Cation compositions per $O_{10}(OH)_2$ of celadonite in the studied samples.

Sr. No.	Tetrahedral Cation		Al (Total)	Octahedral Cation				Interlayer Cation			Total Interlayer Cation
	Si	Al		Al	Mg	Ti	Fe^{3+} (Total)	K	Ca	Na	
Pune											
1	3.90	0.10	0.44	0.34	0.58	0.00	1.00	0.85	0.02	0.01	0.88
2	3.90	0.10	0.43	0.33	0.59	0.00	1.01	0.86	0.01	0.00	0.88
3	3.91	0.09	0.45	0.35	0.56	0.00	1.01	0.86	0.01	0.01	0.88
4	3.90	0.10	0.42	0.32	0.59	0.00	1.02	0.86	0.01	0.01	0.88
5	3.80	0.20	0.50	0.40	0.62	0.00	0.95	0.85	0.02	0.02	0.89
6	3.86	0.14	0.51	0.41	0.64	0.00	0.92	0.85	0.01	0.01	0.87
7	3.89	0.11	0.50	0.40	0.62	0.00	0.91	0.89	0.01	0.01	0.91
8	3.85	0.15	0.43	0.33	0.58	0.00	1.01	0.94	0.01	0.01	0.96
9	3.89	0.11	0.45	0.35	0.60	0.00	0.99	0.83	0.02	0.01	0.86
10	3.89	0.11	0.43	0.33	0.58	0.00	1.03	0.84	0.01	0.02	0.87
11	3.90	0.10	0.43	0.33	0.59	0.00	1.02	0.84	0.01	0.01	0.86
12	3.86	0.14	0.45	0.35	0.54	0.00	1.05	0.81	0.03	0.02	0.85
13	3.86	0.14	0.45	0.35	0.60	0.00	1.00	0.81	0.02	0.02	0.85
14	3.84	0.16	0.41	0.31	0.49	0.00	1.10	0.89	0.03	0.01	0.93
15	3.87	0.13	0.44	0.34	0.60	0.00	1.01	0.82	0.02	0.01	0.85
16	3.96	0.04	0.59	0.49	0.60	0.00	0.83	0.82	0.02	0.01	0.85
17	3.96	0.04	0.53	0.43	0.58	0.00	0.91	0.84	0.01	0.01	0.85
18	3.82	0.18	0.49	0.39	0.64	0.00	0.96	0.84	0.01	0.01	0.86
Salher											
1	3.77	0.23	0.96	0.73	0.46	0.00	0.77	0.70	0.05	0.00	0.75
2	3.89	0.11	0.80	0.69	0.51	0.00	0.75	0.72	0.03	0.00	0.75
3	3.78	0.22	0.99	0.77	0.48	0.00	0.72	0.72	0.03	0.01	0.75
4	3.83	0.17	0.84	0.67	0.51	0.00	0.78	0.72	0.03	0.01	0.76
5	3.77	0.23	0.91	0.68	0.51	0.00	0.79	0.73	0.02	0.00	0.76
6	3.82	0.18	0.92	0.74	0.49	0.00	0.73	0.73	0.03	0.00	0.76
7	3.81	0.19	0.85	0.66	0.54	0.00	0.77	0.73	0.03	0.01	0.76
8	3.78	0.22	0.91	0.69	0.46	0.00	0.81	0.74	0.01	0.01	0.76
9	3.81	0.19	0.93	0.74	0.48	0.00	0.74	0.76	0.01	0.00	0.77
10	3.79	0.21	0.76	0.55	0.51	0.00	0.90	0.74	0.04	0.01	0.79
11	3.86	0.14	0.81	0.67	0.49	0.00	0.78	0.76	0.02	0.01	0.79
12	3.85	0.15	0.81	0.66	0.49	0.00	0.79	0.78	0.01	0.01	0.81
13	3.87	0.13	0.83	0.70	0.42	0.00	0.78	0.79	0.01	0.01	0.81
14	3.84	0.16	0.80	0.64	0.50	0.00	0.80	0.76	0.03	0.00	0.79
15	3.89	0.11	0.74	0.63	0.52	0.00	0.79	0.73	0.03	0.00	0.77
16	3.81	0.19	0.79	0.60	0.52	0.00	0.83	0.79	0.03	0.01	0.82

The average formula of celadonite from Salher was $(K_{0.74}Ca_{0.03}Na_{0.00})_{0.77}$ $(Al_{0.68}Fe^{3+}{}_{0.79}Mg_{0.49})_{1.96}$ $(Si_{3.82}Al_{0.18})_2O_{10}(OH)_{20}$, and that from the Pune green bole was $(K_{0.85}Ca_{0.02}Na_{0.01})_{0.88}$ $(Al_{0.37}Fe^{3+}{}_{0.99}Mg_{0.59})_{1.95}$ $(Si_{3.88}Al_{0.12})_4$ $O_{10}(OH)_2$.

The AIPEA Nomenclature Committee recommended tetrahedral Al substituted for Si^{4+} should range from 0.00 to 0.20 and Si $\geq$ 3.80 atoms per formula unit (a.p.f.u.) in celadonite [3–6,60,84]. The interlayer cation in celadonite should exceed 0.85 a.p.f.u. [3,84,85]. However, the interlayer cation may be less than 0.85 a.p.f.u. in aluminoceladonite [58–60,63,83,86]. Most celadonite data have (IV)Al^{3+} less than 0.20 atom pfu. However, (IV)Al^{3+} value in

celadonite may exceed 0.20 a.p.f.u. [2,13,59,87]. Celadonite from Pune had M^+ more than 0.85 a.p.f.u., but the same from Salher varied from 0.75 to 0.82 a.p.f.u.

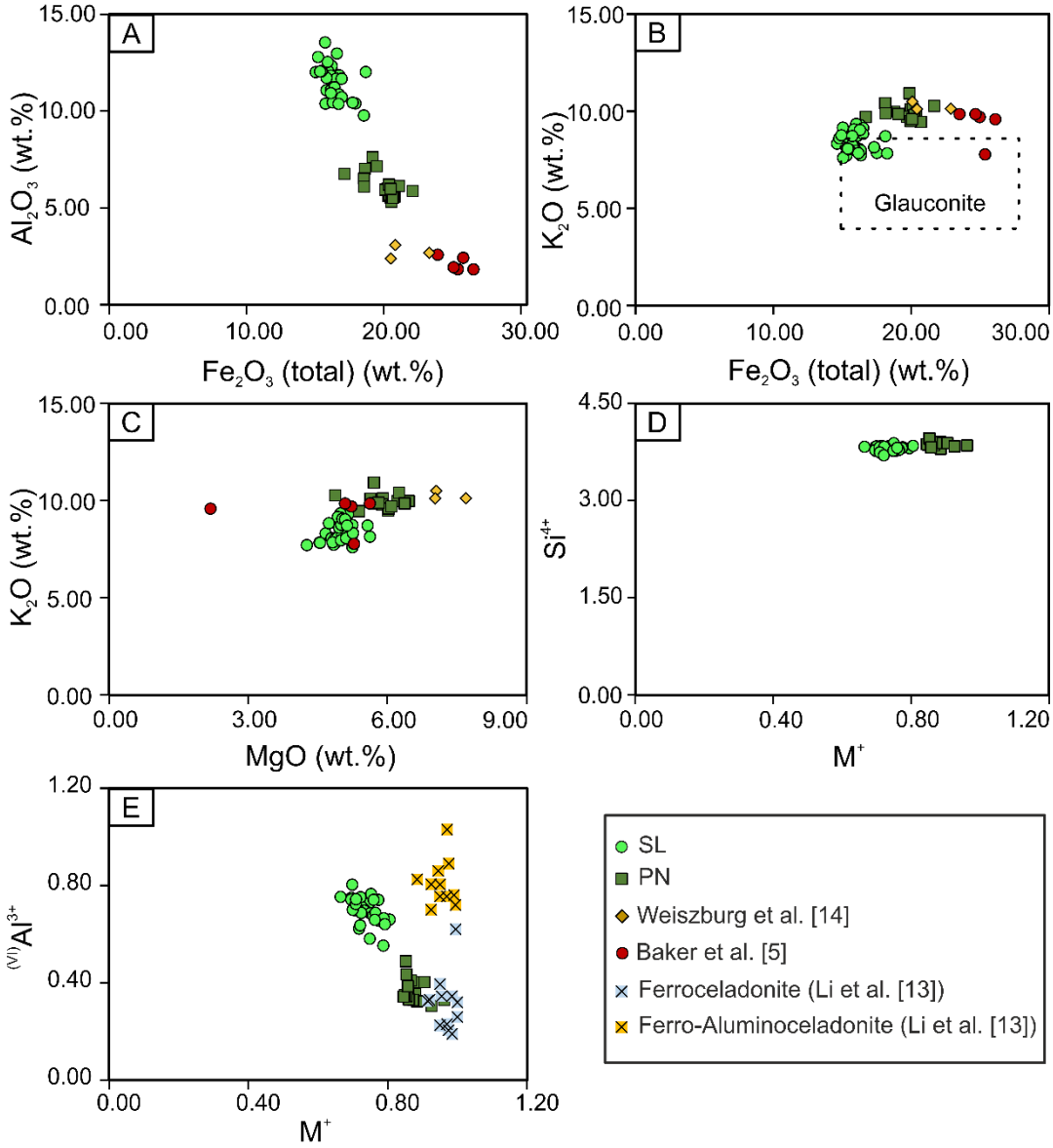

Figure 13. Cross-plots showing chemical differences between celadonite from Salher (SL) and Pune (PN). (**A**) Al_2O_3 vs. Fe_2O_3 (total); (**B**) K_2O vs. Fe_2O_3 (total). The dotted rectangle indicates zone of glauconite as per the data provided in Odin and Matter [88]. The zone above glauconite is marked by celadonite. (**C**) K_2O vs. MgO; (**D**) Si^{4+} vs. M^+ cross-plot. M^+ indicates interlayer cation; i.e., (K+ Ca+ Na). (**E**) Octahedral (VI)Al^{3+} vs. M^+. Celadonites were compared with ferroceladonite and ferro-aluminoceladonites and those reported by Baker et al. [5] and Weiszburg et al. [14].

5. Discussion

5.1. Mineralogical and Chemical Characteristics of the Celadonite in Green Boles

The green authigenic minerals in the Salher and Pune green bole were Fe- and K-containing dioctahedral mica. Mineral chemistry of celadonite overlapped with glauconite in several cases [6,59,89,90]. Therefore, the presence of celadonite in the green boles needed to be confirmed by integrating data using an optical microscope, scanning electron microscope, mineral chemistry, X-ray diffractogram, visible near-infrared spectroscopy, and FTIR spectroscopy.

The celadonite within the studied green boles formed primarily by the dissolution and precipitation mechanism of plagioclase (Figure 3B–D) and glassy phase within volcanic lithic fragments (Figure 3E,F), and as vesicle and intergranular void-filling. However, glauconite is mostly pellet-shaped, formed either by the alteration of fecal pellets, K-feldspar, and quartz, and as precipitates within the bioclasts [88]. Glauconite, containing more than 8 wt % K_2O and more than 25 wt % Fe_2O_3 (total) characterized the highly evolved variety, exhibiting lamellar morphology [3,90–92], whereas, the studied green clay; i.e., celadonite, showed fine (less than 1 µm) euhedral lathlike morphology, which was similar to the celadonite morphology reported in previous studies [3,14,27]. The interlayer cation is one of the criteria to distinguish between mica; i.e., celadonite (interlayer cation more than 0.85 a.p.f.u.), and interlayer deficient mica; i.e., glauconite (interlayer cation less than 0.85 a.p.f.u.) [85]. Although the interlayer cation content of the Pune celadonite exceeded 0.85 a.p.f.u., it varied between 0.75–0.82 a.p.f.u in the case of the Salher celadonite. Therefore, the interlayer cation of the green phase in the Pune green bole satisfied the composition of celadonite, but it was slightly lower in the case of the Salher celadonite. The green clay from both Salher and Pune showed low Al tetrahedral substitution (less than 0.2 a.p.f.u.), which was characteristic of celadonite [1,59,60,83,92]. Further, several studies indicated that the interlayer cation content may be less than 0.85 in the case of aluminoceladonite [59,62,63,83,86]. Therefore, the composition of the primary green phase in the case of the Salher green bole was closer to aluminoceladonite, whereas the same in the case of the Pune green bole was closer to celadonite. X-ray diffraction parameters of the studied samples exhibited sharp hkl reflection, split-up 003 and 022 peaks, and d060 spacing less than 1.51 Å, which was coherent with the XRD data of celadonite reported in the literature. The 1.51 Å d060 value was given as a discriminating value by the AIPEA nomenclature [80]. Unlike celadonite, glauconite exhibits reduced hkl reflection and broader basal peaks than celadonite, as well as merged 003 and 022 peaks and d060 spacing less than 1.51 Å [2,3,11,14,58–61,84]. Therefore, the X-ray diffraction parameters ruled out glauconite and confirmed the presence of celadonite in both green boles. The equally strong metal–OH combination band at ~2.30 µm and 2.35 µm and the strong slope between 1.00 µm and ~2.10 µm under VNIR spectra corroborated the presence of celadonite. In FTIR, celadonite showed sharp stretching and bending vibrations, with characteristic absorbance in OH-stretching region [81–83].

Celadonite composition differed in the green boles of Salher and Pune. The composition of celadonite of the green boles in these places and those reported from other places [5,13,14] were compared (Figure 13). Both Salher and Pune celadonites exhibited higher Al_2O_3 and slightly lower Fe_2O_3 (total) than those reported by Baker et al. [5] and Weiszburg et al. [14]. However, some of the published data of Weiszburg et al. [14] overlapped with the Fe_2O_3 wt % of the studied celadonites. The K_2O and MgO wt % of the studied celadonites overlapped with most of the published data of Baker et al. [5] and Weiszburg et al. [14]. A comparison of the studied celadonites with ferroceladonite and ferroaluminoceladonite data of Li et al. [13] revealed that the Salher celadonite showed lower interlayer cation and higher octahedral Al^{3+} than ferroceladonite, and overlapping octahedral Al^{3+} with ferroaluminoceladonite. Celadonite from Pune partially overlapped with the ferroceladonite data of Li et al. [13]. In addition, the Salher celadonite showed higher Al (total) and lower Fe (total) compared to typical celadonite, and lower Al (total) and higher Fe (total) compared to aluminoceladonite; whereas the Pune celadonite showed a slightly lower value of Fe(total) and a slightly higher value of Al (total) than typical celadonite [59,62,63,83]. The above discussion indicates that the Salher celadonite had a composition closer to ferroaluminoceladonite, and the Pune celadonite was closer to typical celadonite composition.

5.2. Origin of Green Authigenic Celadonite under the Subaerial Condition

Celadonite formation is primarily associated with the submarine alteration of volcaniclastic and intermediate to mafic igneous rocks. However, recent studies suggested

that celadonite can also form in subaerial conditions [4,5]. Unlike celadonite, glauconite is found exclusively in marine deposits, and is extremely rare in the continental setting [90]. The essential elements required for the formation of celadonite are K, Mg, Fe, Al, and Si. The potassium content in the seawater facilitates the alteration of basalt on the seafloor at a low temperature [3–11]. Recent studies showed the formation of this mineral in subaerial conditions as well [4,5,14,15]. It may form along with Fe-smectite during the intermediate stage of alteration of basalt into the soil [4]. Baker et al. [5] suggested the dissolution of glasses in basalt under a closed system as the primary source of K for celadonite formation in the continental setting. The alteration of volcanic rocks by a potassic hydrothermal fluid at the late stage of volcanic activity also forms celadonite [93].

Petrographic investigation of the studied samples demonstrated the formation of celadonite by the partial dissolution of plagioclase and almost complete alteration of pyroxene and olivine along with volcanic glasses in the Salher green bole. Mg, Fe, and Al were released to the pore water because of the dissolution of plagioclase and mafic minerals, whereas potassium was supplied by high-K_2O-containing volcanic glasses. As illustrated by elemental mapping, the alteration of plagioclase into celadonite proceeded with the addition of K, Fe, and Mg (Figure 12D–F) and removal of Al (Figure 12C), with iron oxyhydroxide as a byproduct. Celadonite usually forms in slightly reducing conditions as the altering fluids replace the original substrate [3]. The reducing pore water promoted the substitution of Fe into the silicate structure, rather than forming a separate oxyhydroxide/oxide phase [4,5]. The d003 peak position of celadonite provided an estimation of the oxygen fugacity under which it formed [7,9]. The d003 spacing for celadonite in green boles was 3.31 Å, indicating an oxygen fugacity slightly lower than the hematite-magnetite buffer.

The occurrence of flaky smectite in a few intergranular spaces and within vesicles of glass suggested subsequent enrichment of Fe and Mg under low silica activity (e.g., [4]). The formation of brown smectite within the voids of green celadonite indicated precipitation from a more reducing pore fluid [17,94]. High K_2O and SiO_2 contents in brown-orange and yellow glasses suggested a different source. Contemporaneous volcanic activity to the north possibly supplied felsic ash periodically during the breaks of Deccan Basalts flows (cf. [95,96]). A similar condition was reported in the Grande Ronde Formation, and in sedimentary interbeds between the flows of overlying Columbia River Basalts in central Washington and Picture Gorge subgroup of the Columbia River basalt, Oregon, where anomalously high K contents in paleosols within these basalts corresponded to felsic ash input [29,97]. The alteration of calcic plagioclase; i.e., labradorite into zeolite (heulandite), suggests increased temperature caused by the overlying flow [98–100]. Zeolites in veins and vesicles could form by the late-stage hydrothermal fluid circulation [99,101]. The intergranular pores and veins, filled partially by celadonite, were subsequently occupied by zeolite in the Pune green bole, reflecting rising temperatures during the overlying flow and hydrothermal activity (Figure 5A). The hydrothermal alteration process was responsible for the devitrification of volcanic glass, followed by the hydration and crystallization of the smectite (cf. [102]). The saw-edge-like dissolution feature in pyroxene from the Pune green bole (indicating congruent dissolution) is a common product of weathering in buried truncated volcanic paleosols [103]. Physical, textural, mineralogical, and chemical characteristics of the Salher and Pune green boles showed different characteristics. Field features in Salher suggested the alteration deposition of weathered volcaniclastic in deposit on a local pool of standing water on the undulatory flow top of basalt, whereas the Pune green bole was formed by the in situ alterations of the fragmentary flow top of basalt. The slightly reducing conditions of the formation of the green bole facilitated the retention of Fe^{2+} in the celadonite structure in the subaerial condition in both cases.

The formation of nonmarine celadonite within green boles is important for understanding the paleoenvironmental implications of ancient green mica. During alteration of basic rock in a marine environment, potassium is easily available in the seawater. However, the formation of celadonite in a continental setting requires an alternate source of potassium. One possible source of potassium is felsic volcaniclastic input [14–16]. Understanding the

origin of green mica is crucial for exploring the paleoenvironmental condition of these minerals on the Martian surface [20–28].

6. Conclusions

Detailed petrographical, mineralogical, and geochemical studies made it possible to highlight the following conclusions:

1. Celadonite-bearing green boles were investigated in two study areas of the Late Cretaceous Deccan volcanic province; i.e., Salher and Pune. Green boles were formed by the subaerial alteration of basaltic rocks during the lulls of the eruption of basaltic flows.
2. Combined mineralogical and chemical investigation, as well as VNIR and FTIR spectroscopy, identified the green authigenic mineral as celadonite.
3. Celadonite from the Salher green bole contained slightly lower K_2O (7.90 to ~9 wt %), Fe_2O_3 (total), and MgO, and higher Al_2O_3 contents than those from Pune. The mineral chemistry indicated Salher celadonite was closer to ferro-aluminoceladonite, whereas the Pune celadonite, with a narrow range of K_2O, was closer to typical celadonite composition.
4. The green bole of Salher formed as volcaniclastic deposits in local pools of water on the flow top of basalt under slightly reducing conditions, whereas the green bole in Pune formed by the in situ alteration of the flow top of basalt. The sources of Mg, Fe, and Al of celadonite were linked to the dissolution of pyroxene, plagioclase, and metastable interstitial glasses, respectively; whereas K and Si were contributed by the felsic input in Salher celadonite. K and Si contents of celadonite from Pune were possibly sourced by potassic hydrothermal fluid or groundwater flow.
5. Therefore, this study is important to provide further insight on the formation of authigenic celadonite in a nonmarine environment.

Author Contributions: Conceptualization, P.S., S.B. (Santanu Banerjee), K.P., S.B. (Satadru Bhattacharya); methodology, P.S., K.P., S.S. and E.L.P.; software, P.S., S.B. (Santanu Banerjee); validation, P.S., S.B. (Satadru Bhattacharya); formal analysis, P.S., E.L.P.; investigation, P.S.; resources, S.B. (Santanu Banerjee), K.P.; data curation, P.S., S.S.; writing—original draft preparation, P.S., S.B. (Satadru Bhattacharya); writing—review and editing, K.P., E.L.P.; visualization, S.B. (Santanu Banerjee), E.L.P., K.P.; supervision, S.B. (Satadru Bhattacharya), K.P. and E.L.P.; project administration, S.B. (Santanu Banerjee); funding acquisition, S.B. (Satadru Bhattacharya), K.P. All authors have read and agreed to the published version of the manuscript.

Funding: The study was supported by the SAC and ISRO.

Acknowledgments: The authors are thankful to their host institutes for the infrastructure support. S.B. and K.P. acknowledge financial support from the Space Applications Centre (ISRO) for Project 467 STC0254, entitled "Physico-chemical conditions of formation of bole beds within Deccan basalt for 468 Martian analogue". PSis thankful to CSIR for the fellowship.

Conflicts of Interest: The authors declare no conflict of interest.

Abbreviations

The following abbreviations were used in this manuscript:

VNIR	Visible near-infrared spectroscopy
FTIR	Fourier-transform infrared spectroscopy
MIR	Middle-infrared region spectroscopy
FEG–SEM	Field emission gun–scanning electron microscope
XRD	X-ray diffraction analysis

References

1. Buckley, H.A.; Bevan, J.C.; Brown, K.M.; Johnson, L.R.; Farmer, V.C. Glauconite and celadonite: Two separate mineral species. *Mineral. Mag.* **1978**, *42*, 373–382. [CrossRef]
2. Odom, I.E. Glauconite and celadonite minerals. *Rev. Mineral.* **1984**, *13*, 545–572.

3. Odin, G.S.; Desprairies, A.; Fullagar, P.D.; Bellon, H.; Decarreau, A.; Frohlich, F.; Zelvelder, M. Chapter D nature and geological significance of celadonite. In *Developments in Sedimentology*; Odin, G.S., Ed.; Elsevier: Paris, France, 1988; Volume 45.
4. Velde, B. *Green Clay Minerals. Treatise on Geochemistry*; Elsevier: Amsterdam, The Netherlands, 2003; Volume 7, p. 407.
5. Baker, L.L.; Rember, W.C.; Sprenke, K.F.; Strawn, D.G. Celadonite in continental flood basalts of the Columbia River Basalt Group. *Am. Mineral.* **2012**, *97*, 1284–1290. [CrossRef]
6. Nieto, F.; Abad, I.; Bauluz, B.; Reolid, M. Textural and genetic relationships between glauconite and celadonite at the nanoscale: Two different structural-compositional fields. *Eur. J. Mineral.* **2021**, *33*, 503–517. [CrossRef]
7. Wise, W.S.; Eugster, H.P. Celadonite: Synthesis, thermal stability and occurrence. *Am. Mineral.* **1964**, *49*, 1031–1083.
8. Kohyama, N.; Shimoda, S.; Sudo, T. Celadonite in the Tuff of Oya, Tochigi Prefecture, Japan. *Mineral. J.* **1971**, *6*, 299–312. [CrossRef]
9. Andrews, A.J. Saponite and celadonite in layer 2 basalts, DSDP Leg 37. *Contrib. Mineral. Petrol.* **1980**, *73*, 323–340. [CrossRef]
10. Staudigel, H.; Gillis, K.; Duncan, R. K/Ar and Rb/Sr ages of celadonites from the Troodos ophiolite, Cyprus. *Geology* **1986**, *14*, 72–75. [CrossRef]
11. Giorgetti, G.; Marescotti, P.; Cabella, R.; Lucchetti, G. Clay mineral mixtures as alteration products in pillow basalts from the eastern flank of Juan de Fuca Ridge: A TEM-AEM study. *Clay Miner.* **2001**, *36*, 75–91. [CrossRef]
12. Boles, J.R.; Coombs, D.S. Mineral reactions in zeolitic Triassic tuff, Hokonui Hills, New Zealand. *Geol. Soc. Am. Bull.* **1975**, *86*, 163–173. [CrossRef]
13. Li, G.; Peacor, D.R.; Coombs, D.S.; Kawachi, Y. Solid solution in the celadonite family: The new minerals ferroceladonite, $K_2Fe^{2+}{}_2Fe^{3+}{}_3Si_8O_{20}(OH)_4$, and ferroaluminoceladonite, $K_2Fe^{2+}{}_2Al_2Si_8O_{20}(OH)_4$. *Am. Mineral.* **1997**, *82*, 503–511. [CrossRef]
14. Weiszburg, T.G.; Tóth, E.; Beran, A. Celadonite, the 10-Å green clay mineral of the manganese carbonate ore, Úrkút, Hungary. *Acta Mineral.-Petrogr.* **2004**, *45*, 65–80.
15. Tóth, E.; Weiszburg, T.G.; Jeffries, T.; Williams, C.T.; Bartha, A.; Bertalan, É.; Cora, I. Submicroscopic accessory minerals overprinting clay mineral REE patterns (celadonite–glauconite group examples). *Chem. Geol.* **2010**, *269*, 312–328. [CrossRef]
16. Savko, K.A.; Piliugin, S.M.; Bazikov, N.S. Experimental data for high-temperature decomposition of natural celadonite from banded iron formation. *Chin. J. Geochem.* **2015**, *34*, 507–514. [CrossRef]
17. Polgári, M.; Hein, J.R.; Németh, T.; Pál-Molnár, E.; Vigh, T. Celadonite and smectite formation in the Úrkút Mn-carbonate ore deposit (Hungary). *Sediment. Geol.* **2013**, *294*, 157–163. [CrossRef]
18. Polgári, M.P.; Gyollai, I. Geochemical constraints on the element enrichments of microbially mediated manganese and iron ores—An overview. *Ore Geol. Rev.* **2021**, *136*, 104203. [CrossRef]
19. Loveland, P.J.; Bendelow, V.C. Celadonite-aluminous-glauconite: An example from the Lake District, UK. *Mineral. Mag.* **1984**, *48*, 113–117. [CrossRef]
20. Polgári, M.; Hein, J.R.; Tóth, A.L.; Pál-Molnár, E.; Vigh, T.; Bíró, L.; Fintor, K. Microbial action formed Jurassic Mn-carbonate ore deposit in only a few hundred years (Úrkút, Hungary). *Geology* **2012**, *40*, 903–906. [CrossRef]
21. Wilson, M.J.; Deer, W.A.; Howie, R.A.; Zussman, J. *Rock-Forming Minerals, Volume 3C, Sheet Silicates: Clay Minerals*; Geological Society: London, UK, 2013.
22. Bishop, J.L.; Lane, M.D.; Dyar, M.D.; Brown, A.J. Reflectance and emission spectroscopy study of four groups of phyllosilicates: Smectites, kaolinite-serpentines, chlorites and micas. *Clay Miner.* **2008**, *43*, 35–54. [CrossRef]
23. Craig, P.; Chevrier, V.; Sayyed, M.R.G.; Islam, R. Spectral analysis of Deccan intrabasaltic bole beds: Implications for the formation and alteration of phyllosilicates on Mars. *Planet. Space Sci.* **2017**, *135*, 55–63. [CrossRef]
24. Ehlmann, B.L.; Edwards, C.S. Mineralogy of the Martian Surface. *Annu. Rev. Earth Planet. Sci.* **2014**, *42*, 408. [CrossRef]
25. Ehlmann, B.L.; Berger, G.; Mangold, N.; Michalski, J.R.; Catling, D.C.; Ruff, S.V.; Chassefière, E.; Niles, P.B.; Chevrier, V.; Poulet, F. Geochemical consequences of widespread clay mineral formation in Mars' Ancient Crust. *Space Sci. Rev.* **2013**, *174*, 329–364. [CrossRef]
26. Rampe, E.B.; Blake, D.F.; Bristow, T.F.; Ming, D.W.; Vaniman, D.T.; Morris, R.V.; Achilles, C.N.; Chipera, S.J.; Morrison, S.M.; Tu, V.M.; et al. Mineralogy and geochemistry of sedimentary rocks and eolian sediments in Gale crater, Mars: A review after six Earth years of exploration with Curiosity. *Geochemistry* **2020**, *80*, 125605. [CrossRef]
27. Tangari, A.C.; Marinangeli, L.; Scarciglia, F.; Pompilio, L.; Piluso, E. Volcanic holocrystalline bedrock and hydrothermal alteration: A terrestrial analogue for Mars. *Minerals* **2020**, *10*, 1082. [CrossRef]
28. Losa-Adams, E.; Gil-Lozano, C.; Fairén, A.G.; Bishop, J.L.; Rampe, E.B.; Gago-Duport, L. Long-lasting habitable periods in Gale crater constrained by glauconitic clays. *Nat. Astron.* **2021**, *5*, 936–942. [CrossRef] [PubMed]
29. Singer, A.; Ben-Dor, E. Origin of red clay layers interbedded with basalts of the Golan Heights. *Geoderma* **1987**, *39*, 293–306. [CrossRef]
30. Singer, A.; Wieder, M.; Gvirtzman, G. Paleoclimate deduced from some early Jurassic basalt-derived paleosols from northern Israel. *Palaeogeogr. Palaeoclimatol. Palaeoecol.* **1994**, *111*, 73–82. [CrossRef]
31. Sheldon, N.D. Pedogenesis and geochemical alteration of the Picture Gorge subgroup, Columbia River basalt, Oregon. *Geol. Soc. Am. Bull.* **2003**, *115*, 1377–1387. [CrossRef]
32. Ghosh, P.; Sayeed, M.R.G.; Islam, R.; Hundekari, S.M. Inter-basaltic clay (bole bed) horizons from Deccan traps of India: Implications for palaeo-weathering and palaeo-climate during Deccan volcanism. *Palaeogeogr. Palaeoclimatol. Palaeoecol.* **2006**, *242*, 90–109. [CrossRef]
33. Chenet, A.L.; Fluteau, F.; Courtillot, V.; Gérard, M.; Subbarao, K.V. Determination of rapid Deccan eruptions across the Cretaceous-Tertiary boundary using paleomagnetic secular variation: Results from a 1200-m-thick section in the Mahabaleshwar escarpment. *J. Geophys. Res. Solid Earth* **2008**, *113*. [CrossRef]

34. Mitchell, R.L.; Sheldon, N.D. Weathering and paleosol formation in the 1.1 Ga Keweenawan Rift. *Precambrian Res.* **2009**, *168*, 271–283. [CrossRef]
35. Jutras, P.; Hanley, J.J.; Quillan, R.S.; Leforte, M.J. Intra-basaltic soil formation, sedimentary reworking and eodiagenetic K-enrichment in the Middle to Upper Ordovician Dunn Point Formation of eastern Canada: A rare window into early Palaeozoic surface and near-surface conditions. *Geol. Mag.* **2012**, *149*, 798–818. [CrossRef]
36. Srivastava, P.; Sangode, S.J.; Meshram, D.C.; Gudadhe, S.S.; Nagaraju, E.; Kumar, A.; Venkateshwarlu, M. Paleoweathering and depositional conditions in the inter-flow sediment units (bole beds) of Deccan Volcanic Province, India: A mineral magnetic approach. *Geoderma* **2012**, *177*, 90–109. [CrossRef]
37. Srivastava, P.; Sangode, S.J.; Torrent, J. Mineral magnetic and diffuse reflectance spectroscopy characteristics of the Deccan volcanic bole beds: Implications to genesis and transformations of iron oxides. *Geoderma* **2015**, *239*, 317–330. [CrossRef]
38. Spinola, D.N.; de Castro Portes, R.; Schaefer, C.E.G.R.; Solleiro-Rebolledo, E.; Pi-Puig, T.; Kühn, P. Eocene paleosols on King George Island, Maritime Antarctica: Macromorphology, micromorphology and mineralogy. *Catena* **2017**, *152*, 69–81. [CrossRef]
39. Singh, P.; Le Pera, E.; Bhattacharya, S.; Pande, K.; Banerjee, S. Mineralogical and Textural Characteristics of Red Boles of Western Deccan Volcanic Province, India: Genetic and Paleoenvironmental Implications. In *Mesozoic Stratigraphy of India*; Banerjee, S., Sarkar, S., Eds.; Society of Earth Scientists Series; Springer: Cham, Switzerland, 2021; Volume 1, pp. 697–722. [CrossRef]
40. Sayyed, M.R.G.; Hundekari, S.M. Preliminary comparison of ancient bole beds and modern soils developed upon the Deccan volcanic basalts around Pune (India): Potential for palaeoenvironmental reconstruction. *Quat. Int.* **2006**, *156*, 189–199. [CrossRef]
41. Greenberger, R.N.; Mustard, J.F.; Kumar, P.S.; Dyar, M.D.; Breves, E.A.; Sklute, E.C. Low temperature aqueous alteration of basalt: Mineral assemblages of Deccan basalts and implications for Mars. *J. Geophys. Res. Planets* **2012**, *117*, E11. [CrossRef]
42. Wadia, D.N. *Geology of India*, 4th ed.; Tata-McGraw Hill: New Delhi, India, 1975; p. 508.
43. Sheth, H.C. From Deccan to Réunion: No trace of a mantle plume. *Spec. Pap. Geol. Soc. Am.* **2005**, *388*, 477–501.
44. Vaidyanadhan, R.; Ramakrishan, M. *Geology of India*; Geological Society of India: Bangalore, India, 2008; Volume 2, p. 994.
45. Pande, K. Age and duration of the Deccan Traps, India: A review of radiometric and paleomagnetic constraints. *J. Earth Syst. Sci.* **2002**, *111*, 115. [CrossRef]
46. Kale, V.S.; Bodas, M.; Chatterjee, P.; Pande, K. Emplacement history and evolution of the Deccan Volcanic Province, India. *Episodes* **2020**, *43*, 278–299. [CrossRef]
47. Kale, V.S.; Dole, G.; Shandilya, P.; Pande, K. Stratigraphy and correlations in Deccan Volcanic Province, India: Quo vadis? *Geol. Soc. Am. Bull.* **2019**, *132*, 588–607. [CrossRef]
48. Duraiswami, R.A.; Sheth, H.; Gadpallu, P.; Youbi, N.; Chellai, E.H. A simple recipe for red bole formation in continental flood basalt provinces: Weathering of flow-top and flow-bottom breccias. *Arab. J. Geosci.* **2020**, *13*, 953. [CrossRef]
49. Chenet, A.L.; Courtillot, V.; Fluteau, F.; Gérard, M.; Quidelleur, X.; Khadri, S.F.R.; Subbarao, K.V.; Thordarson, T. Determination of rapid Deccan eruptions across the Cretaceous-Tertiary boundary using paleomagnetic secular variation: 2. Constraints from analysis of eight new sections and synthesis for a 3500 m thick composite section. *J. Geophys. Res. Solid Earth* **2009**, *114*. [CrossRef]
50. Beane, J.E.; Turner, C.A.; Hooper, P.R.; Subbarao, K.V.; Walsh, J.N. Stratigraphy, composition and form of the Deccan basalts, Western Ghats, India. *Bull. Volcanol.* **1986**, *48*, 61–83. [CrossRef]
51. Subbarao, K.V.; Hopper, P.R. Reconnaissance map of the Deccan Basalt Group in the Western Ghats, India. In *Deccan Flood Basalts*; Subbarao, K.V., Ed.; Geological Society of India Memoir: Bangalore, India, 1988; Volume 10.
52. Subbarao, K.V.; Chandrasekharam, D.; Navaneethakrishnan, P.; Hooper, P.R. Stratigraphy and structure of parts of the Central Deccan basalt province: Eruptive models. In *Volcanism*; Subbarao, K.V., Ed.; Wiley Eastern Ltd.: New Delhi, India, 1994; pp. 321–332.
53. Chipera, S.J.; Bish, D.L. Effects of humidity on clay and zeolite quantitative XRD analyses. In Proceedings of the 30th Annual Clay Minerals Society Meeting, San Diego, CA, USA, 25–29 July 1993; p. 53.
54. Soukup, D.A.; Buck, B.J.; Harris, W. Preparing soils for mineralogical analyses. In *Methods of Soil Analysis Part 5—Mineralogical Methods*; Soil Science Society of America: Madison, WI, USA, 2008; Volume 5, pp. 13–31. [CrossRef]
55. Moore, D.M.; Reynolds, R.C., Jr. *X-ray Diffraction and the Identification and Analysis of Clay Minerals*; Oxford University Press (OUP): Oxford, UK, 1989.
56. Bhattacharya, S.; Mitra, S.; Gupta, S.; Jain, N.; Chauhan, P.; Parthasarathy, G. Jarosite occurrence in the Deccan Volcanic Province of Kachchh, western India: Spectroscopic studies on a Martian analog locality. *J. Geophys. Res. Planets* **2016**, *121*, 402–431. [CrossRef]
57. Naveen Sarkar, S.; Kumar, T.N.; Ray, D.; Bhattacharya, S.; Shukla, A.D.; Moitra, H.; Dagar, A.; Chauhan, P.; Sen, K.; Das, S. Mineralogy and spectroscopy (VIS near infrared and micro-Raman) of chromite from Nidar ophiolite complex, SE Ladakh, India: Implications for future planetary exploration. *Planet. Space Sci.* **2019**, *165*, 1–9. [CrossRef]
58. Hradil, D.; Píšková, A.; Hradilová, J.; Bezdička, P.; Lehrberger, G. and Gerzer, S. Mineralogy of Bohemian green earth pigment and its microanalytical evidence in historical paintings. *Archaeometry* **2011**, *53*, 563–586. [CrossRef]
59. Zviagina, B.B.; Drits, V.A.; Sakharov, B.A.; Ivanovskaya, T.A.; Dorzhieva, O.V.; McCarty, D.K. Crystal-chemical regularities and identification criteria in Fe-bearing, K-dioctahedral 1M micas from X-ray diffraction and infrared spectroscopy data. *Clays Clay Miner.* **2017**, *65*, 234–251. [CrossRef]
60. Zviagina, B.B.; Drits, V.A.; Środoń, J.; McCarty, D.K.; Dorzhieva, O.V. The illite–aluminoceladonite series: Distinguishing features and identification criteria from X-ray diffraction and infrared spectroscopy data. *Clays Clay Miner.* **2015**, *63*, 378–394. [CrossRef]
61. Schmidt, S.T.; Süssenberger, A.; Wemmer, K. Posteruptive Thermal History of the Proterozoic Basaltic North Shore Volcanic Group of the Midcontinent Rift: Evidence from K/Ar Data of Celadonite. *Lithosphere* **2021**, *2021*, 8836546. [CrossRef]

62. Reid, D.A.; Graham, R.C.; Edinger, S.B.; Bowen, L.H.; Ervin, J.O. Celadonite and its transformation to smectite in an Entisol at Red Rock Canyon, Kern County, California. *Clays Clay Miner.* **1988**, *36*, 425–431. [CrossRef]
63. Drits, V.A.; Zviagina, B.B.; McCarty, D.K.; Salyn, A.L. Factors responsible for crystal-chemical variations in the solid solutions from illite to aluminoceladonite and from glauconite to celadonite. *Am. Mineral.* **2010**, *95*, 348–361. [CrossRef]
64. Sakharov, B.A.; Besson, G.; Drits, V.A.; Kameneva, M.Y.; Salyn, A.L.; Smoliar, B.B. X-ray study of the nature of stacking faults in the structure of glauconites. *Clay Miner.* **1990**, *25*, 419–435. [CrossRef]
65. Burns, R.G. *Mineralogical Applications of Crystal-Field Theory*; Cambridge University Press: Cambridge, UK, 1993; Volume 551. [CrossRef]
66. Clark, R.N.; King, T.V.; Klejwa, M.; Swayze, G.A.; Vergo, N. High spectral resolution reflectance spectroscopy of minerals. *J. Geophys. Res. Solid Earth* **1990**, *95*, 12653–12680. [CrossRef]
67. Bishop, J.L.; Pieters, C.M.; Edwards, J.O. Infrared spectroscopic analyses on the nature of water in montmorillonite. *Clays Clay Miner.* **1994**, *42*, 702–716. [CrossRef]
68. Bishop, J.; Madejova, J.; Komadel, P.; Froschl, H. The influence of structural Fe, Al and Mg on the infrared OH bands in spectra of dioctahedral smectites. *Clay Miner.* **2002**, *37*, 607–616. [CrossRef]
69. Ehlmann, B.L.; Bish, D.L.; Ruff, S.W.; Mustard, J.F. Mineralogy and chemistry of altered Icelandic basalts: Application to clay mineral detection and understanding aqueous environments on Mars. *J. Geophys. Res. Planets* **2012**, *117*. [CrossRef]
70. Bishop, J.; Murad, E.; Dyar, M.D. The influence of octahedral and tetrahedral cation substitution on the structure of smectites and serpentines as observed through infrared spectroscopy. *Clay Miner.* **2002**, *37*, 617–628. [CrossRef]
71. Frost, R.L.; Kloprogge, J.T.; Ding, Z. Near-infrared spectroscopic study of nontronites and ferruginous smectite. *Spectrochim. Acta A Mol. Biomol. Spectrosc.* **2002**, *58*, 1657–1668. [CrossRef]
72. Ehlmann, B.L.; Mustard, J.F.; Swayze, G.A.; Clark, R.N.; Bishop, J.L.; Poulet, F.; Des Marais, D.J.; Roach, L.H.; Milliken, R.E.; Wray, J.J.; et al. Identification of hydrated silicate minerals on Mars using MRO-CRISM: Geologic context near Nili Fossae and implications for aqueous alteration. *J. Geophys. Res. Planets* **2009**, *114*. [CrossRef]
73. Fanost, A.; Gimat, A.; de Viguerie, L.; Martinetto, P.; Giot, A.C.; Clémancey, M.; Blondin, G.; Gaslain, F.; Glanville, H.; Walter, P.; et al. Revisiting the identification of commercial and historical green earth pigments. *Colloids Surf. A Physicochem. Eng. Asp.* **2020**, *584*, 124035. [CrossRef]
74. Bishop, J.L.; Perry, K.A.; Darby Dyar, M.; Bristow, T.F.; Blake, D.F.; Brown, A.J.; Peel, S.E. Coordinated spectral and XRD analyses of magnesite-nontronite-forsterite mixtures and implications for carbonates on Mars. *J. Geophys. Res. Planets* **2013**, *118*, 635–650. [CrossRef]
75. Cariati, F.; Erre, L.; Micera, G.; Piu, P.; Gessa, C. Water molecules and hydroxyl groups in montmorillonites as studied by near infrared spectroscopy. *Clays Clay Miner.* **1981**, *29*, 157–159. [CrossRef]
76. Bishop, J.L.; Dobrea, E.Z.N.; McKeown, N.K.; Parente, M.; Ehlmann, B.L.; Michalski, J.R.; Milliken, R.E.; Poulet, F.; Swayze, G.A.; Mustard, J.F.; et al. Phyllosilicate diversity and past aqueous activity revealed at Mawrth Vallis, Mars. *Science* **2008**, *321*, 830–833. [CrossRef] [PubMed]
77. Grauby, O.; Petit, S.; Decarreau, A.; Baronnet, A. The nontronite-saponite series: An experimental approach. *Eur. J. Mineral.* **1994**, 99–112. [CrossRef]
78. Gates, W. Infrared spectroscopy and the chemistry of dioctahedral smectites. In *The Application of Vibrational Spectroscopy of Layer Silicates and Hydroxides*; Kloprogge, J.T., Ed.; The Clay Minerals Society: Aurora, CO, USA, 2005; pp. 126–168. [CrossRef]
79. Slonimskaya, M.V.; Besson, G.; Dainyak, L.G.; Tchoubar, C.; Drits, V.A. Interpretation of the IR spectra of celadonites and glauconites in the region of OH-stretching frequencies. *Clay Miner.* **1986**, *21*, 377–388. [CrossRef]
80. Besson, G.; Drits, V.A. Refined relationships between chemical composition of dioctahedral fine-grained mica minerals and their infrared spectra within the OH stretching region. Part I: Identification of the OH stretching bands. *Clays Clay Miner.* **1997**, *45*, 158–169. [CrossRef]
81. Moretto, L.M.; Orsega, E.F.; Mazzocchin, G.A. Spectroscopic methods for the analysis of celadonite and glauconite in Roman green wall paintings. *J. Cult. Herit.* **2011**, *12*, 384–391. [CrossRef]
82. Farmer, V.C. The layer silicate. In *The Infrared Spectra of Minerals. Monograph 4*; Farmer, V.C., Ed.; Mineral Society: London, UK, 1974; pp. 331–364.
83. Zviagina, B.B.; Drits, V.A.; Dorzhieva, O.V. Distinguishing features and identification criteria for K-dioctahedral 1M micas (Illite-aluminoceladonite and illite-glauconite-celadonite series) from middle-infrared spectroscopy data. *Minerals* **2020**, *10*, 153. [CrossRef]
84. Bailey, S.W. Summary of recommendations of AIPEA nomenclature committee on clay minerals. *Clay Miner.* **1980**, *15*, 85–93. [CrossRef]
85. Rieder, M.; Cavazzini, G.; D'yakonov, Y.S.; Frank-Kamenetskii, V.A.; Gottardi, G.; Guggenheim, S.; Koval, P.V.; Mueller, G.; Neiva, A.M.; Radoslovich, E.W.; et al. Nomenclature of the micas. *Clays Clay Miner.* **1998**, *46*, 586–595. [CrossRef]
86. Kądziołka-Gaweł, M.; Czaja, M.; Dulski, M.; Krzykawski, T.; Szubka, M. Impact of high temperatures on aluminoceladonite studied by Mössbauer, Raman, X-ray diffraction and X-ray photoelectron spectroscopy. *Mineral. Petrol.* **2021**, *115*, 431–444. [CrossRef]
87. Weaver, C.E.; Pollard, L.D. *The Chemistry of Clay Minerals*; Elsevier: Amsterdam, The Netherlands, 1973; pp. 5–53.
88. Odin, G.S.; Matter, A. De glauconiarum origine. *Sedimentology* **1981**, *28*, 611–641. [CrossRef]
89. López-Quirós, A.; Sánchez-Navas, A.; Nieto, F.; Escutia, C. New insights into the nature of glauconite. *Am. Miner.* **2020**, *105*, 674–686. [CrossRef]
90. Chattoraj, S.L.; Banerjee, S.; Saraswati, P.K.; Bansal, U. Origin, depositional setting and stratigraphic implications of Palaeogene glauconite of Kutch. *Spec. Publ. Geol. Soc. India* **2016**, *6*, 75–88. [CrossRef]

91. Choudhury, T.R.; Banerjee, S.; Khanolkar, S.; Saraswati, P.K.; Meena, S.S. Glauconite authigenesis during the onset of the Paleocene-Eocene Thermal Maximum: A case study from the Khuiala Formation in Jaisalmer Basin, India. *Palaeogeogr. Palaeoclimatol. Palaeoecol.* **2021**, *571*, 110388. [CrossRef]
92. Duplay, J.; Buatier, M. The problem of differentiation of glauconite and celadonite. *Chem. Geol.* **1990**, *84*, 264–266. [CrossRef]
93. French, W.J.; Hassan, M.D.; Westcott, J.E. A celadonite-vermiculite series from the volcanic rocks of the Ochils, Stirlingshire. *Mineral. Mag.* **1977**, *41*, 481–485. [CrossRef]
94. Polgári, M.; Hein, J.R.; Vigh, T.; Szabó-Drubina, M.; Fórizs, I.; Bíró, L.; Müller, A.; Tóth, A.L. Microbial processes and the origin of the Úrkút manganese deposit, Hungary. *Ore Geol. Rev.* **2012**, *47*, 87–109. [CrossRef]
95. Schoene, B.; Samperton, K.M.; Eddy, M.P.; Keller, G.; Adatte, T.; Bowring, S.A.; Khadri, S.F.; Gertsch, B. U-Pb geochronology of the Deccan Traps and relation to the end-Cretaceous mass extinction. *Science* **2015**, *347*, 182–184. [CrossRef] [PubMed]
96. O'Connor, L.; Szymanowski, D.; Eddy, M.P.; Samperton, K.M.; Schoene, B. A red bole zircon record of cryptic silicic volcanism in the Deccan Traps, India. *Geology* **2022**. [CrossRef]
97. Jolley, D.W.; Widdowson, M.; Self, S. Volcanogenic nutrient fluxes and plant ecosystems in large igneous provinces: An example from the Columbia River Basalt Group. *J. Geol. Soc. Lond.* **2008**, *165*, 955–966. [CrossRef]
98. Deer, W.A.; Howie, R.A.; Zussman, J. *An Introduction to the Rock Forming Minerals*; Longman Group Ltd.: London, UK, 1966; p. 528.
99. Gottardi, G. The genesis of zeolites. *Eur. J. Mineral.* **1989**, 479–488. [CrossRef]
100. Iijima, A. Occurrence of natural zeolites. *J. Clay Sci. Soc. Jpn.* **1986**, *26*, 90–103. [CrossRef]
101. Hall, A. Zeolitization of volcaniclastic sediments; the role of temperature and pH. *J. Sediment. Res.* **1998**, *68*, 739–745. [CrossRef]
102. García-Romero, E.; Vegas, J.; Baldonedo, J.L.; Marfil, R. Clay minerals as alteration products in basaltic volcaniclastic deposits of La Palma (Canary Islands, Spain). *Sediment. Geol.* **2005**, *174*, 237–253. [CrossRef]
103. Sedov, S.; Stoops, G.; Shoba, S. Regoliths and soils on volcanic ash. In *Interpretation of Micromorphological Features of Soils and Regoliths*; Stoops, G., Marcelino, V., Mees, F., Eds.; Elsevier: Amsterdam, The Netherlands, 2010; pp. 275–303. [CrossRef]